Penetration of convective plumes into a stably stratified layer: turbulent mixing & tracer transport

Charles Powell

Supervisors: Peter H. Haynes & John R. Taylor

January 2023

Submitted for the Smith-Knight / Rayleigh-Knight Prizes 2023

Abstract

Intense thunderstorms in the equatorial lower atmosphere can occasionally overshoot into the stratosphere, carrying small amounts of water vapour with them and irreversibly hydrating the surrounding environment. As one of the primary possible pathways for vertical transport of water vapour into the middle atmospheric layer, it is important to understand and quantify the processes resulting in irreversible transport. We reduce the problem to understanding the mixing that occurs as a convective plume of fluid penetrates a stable layer, emulating the atmospheric setup. By neglecting complicating factors such as the large-scale atmospheric flow, intra-cloud processes and thermodynamics, the essential mechanisms are more easily studied and interpreted. In this essay we explore the dynamics of the turbulent flow in a fluid plume rising from a source of buoyancy, first in a uniform environment, then with the introduction of a stratified layer in which the fluid density decreases linearly with height. The central questions of this problem are how much tracer is carried to regions with active mixing between the plume and environment, how much actually mixes with the environment, and how much tracer therefore remains in the stable layer? To that end, we explore the distribution of tracer across fluid parcels with a range of buoyancy, in particular presenting a method of distinguishing volumes of plume fluid which have mixed with the environment from those which have not. We also discuss methods of visualising and characterising the turbulent mixing between the plume and environmental fluid, focusing on metrics which quantify the intensity and efficiency of mixing. Finally, we discuss possible routes from the aforementioned analyses to a quantitative model applicable to the original stratospheric hydration problem.

Statement of originality. This essay contains original work insofar as it uses the quoted references and except as acknowledged below. Sections 2.1, 3.4, 6.1 and 6.2 contain review material. Section 2 utilises definitions from, and makes comparison with, van Reeuwijk et al. (2016) and Craske (2016). Sections 3.2 and 3.3 compare my own numerical simulations with those of Ansong and Sutherland (2010), making reference to their results and emulating certain measurement techniques. Section 4.2 builds on the buoyancy-tracer joint PDF used by Penney et al. (2020), with important differences that are made clear in the text. The remainder of this essay constitutes original research.

This research was conducted under the guidance of my PhD supervisors, Peter Haynes & John Taylor, both of whom have offered invaluable advice throughout and provided comments during the preparation of this essay. I would also like to acknowledge useful discussions with Aaron Wienkers during development of the numerical simulations used in this research.

1 Introduction

In the tropical upper troposphere and lower stratosphere (UTLS), convective plumes generated by strong thunderstorm complexes can penetrate through the tropical tropopause layer (TTL) into the lower stratosphere. Stratospheric composition is largely set by cross-tropopause transport in the tropics as tropospheric air predominantly enters the stratosphere in the tropics (Fueglistaler et al., 2009). There is an ongoing debate on the importance of convective penetration in this transport, particularly with respect to water vapour, where it may allow the local temperature constraint on concentrations to be avoided and lead to a hydrating effect (Jensen et al., 2007). There exists numerical simulations of convective penetration events in complex meteorological models (Dauhut et al., 2015, 2018) containing many physical processes but this is computationally expensive and more challenging to interpret. In this project, the working hypothesis is that the process of convective penetration in the UTLS itself can be greatly simplified by considering a simple fluid dynamical problem representative of the TTL, in which a region of strong stable stratification is penetrated by a turbulent buoyant plume generated in a region with weak or zero stable stratification.

We neglect many complicating factors such as shear in the strongly stably stratified layer, the thermodynamics of distinct phases of water, and associated latent heating in favour of a passive tracer and a quiescent environment. The simplified nature of the problem is expected to make investigation of passive tracer transport and mixing clearer and aid the development of models of this transport as a function of characteristic plume quantities. The effect of complicating factors on transport can then be considered later, by directly introducing shear, or via simple parameterisations of thermodynamic effects such as saturation and sublimation using multiple tracers. Further, the fluid dynamical problem of convective penetration itself is of continuing scientific interest in the literature, in particular the generation of gravity waves by the penetrating plume cap and the energetics of the system, with applications to many problems. It has only recently become possible to numerically simulate this problem at mid to high resolution, owing to constraints such as the domain size needed to control edge effects, among others.

In this essay we focus on developing methods of analysing the turbulent mixing and the associated passive tracer transport, rather than presenting results on the dependence of these processes on the stratification strength, which will be the immediate focus of our future work. Here, we work towards a general picture of the mixing characteristics in convective penetration, so that we may understand what changes when the stratification strength is varied. First, we explore the dynamics of a buoyant plume in an unstratified environment, then with a linearly stably stratified environment overlying an unstratified layer of fixed depth where the plume is generated. We then consider methods of visualising the tracer distribution in buoyancy space and identify the changes that result from mixing between the plume and environment. A method of identifying plume fluid which has mixed with the environment is developed, by extending the buoyancy-tracer joint PDF utilised in Penney et al. (2020) with a correction for the buoyancy-tracer distribution which enters the control volume and utilising transport properties of mixing and stirring in buoyancy-tracer space. This is the central result of this essay; the segregated volume distribution allows consideration of the changing characteristics of plume fluid before and after mixing with the environment (which we will refer to as pre- and post-mixed), and provides a basis for comparing the penetration problem under varied stratification strength. We then discuss the characteristics of pre- and post-mixed fluid in the context of metrics which quantify the intensity, efficiency and mechanism of mixing, demonstrating a way to exploit the segregated volume distribution method. Finally, we briefly discuss ideas which will take the research presented in this essay further.

2 Unstratified plume dynamics

In this section we explore the canonical theory for the dynamics of a plume in an unstratified environment. We then detail the numerical methods used for simulating such a plume, and use the results of one of these high resolution simulations to understand the turbulent dynamics of a simple buoyant plume. This provides a basis for understanding the essential physics of a turbulent plume which we will use throughout the remainder of this essay.

2.1 Canonical plume theory

A buoyant plume is the shear-free flow resulting from a localised and continuous source of buoyancy. A 'forced' plume has non-zero source momentum whilst a 'pure' plume has none. The canonical theory of plumes pioneered by Morton et al. (1956) (henceforth MTT) is centred on a self-similarity hypothesis: far from the source and ignoring molecular effects, velocity and buoyancy collapse onto a single profile when normalised by characteristic scales r_m, w_m, b_m. These scales are defined with respect to the integral buoyancy flux, momentum flux, and volume flux F, M, Q associated with the plume, as well as the integral buoyancy B, collectively referred to as integral quantities. We have

$$r_m \equiv \frac{Q}{M^{1/2}}, \quad w_m \equiv \frac{M}{Q}, \quad b_m \equiv \frac{BM}{Q^2} = \frac{B}{r_m^2} = \frac{F}{\theta_m Q} \tag{1}$$

where

$$Q \equiv 2\int_0^\infty \overline{w} r \,\mathrm{d}r, \quad M \equiv 2\int_0^\infty \overline{w}^2 r \,\mathrm{d}r, \quad B \equiv 2\int_0^\infty \overline{b} r \,\mathrm{d}r, \quad F \equiv \int_0^\infty \overline{w}\overline{b} r \,\mathrm{d}r \tag{2}$$

These integral quantities naturally arise from radially integrating the Boussinesq equations for conservation of mass, momentum, buoyancy and energy. The resulting equations govern the vertical evolution of these fluxes:

$$\frac{\mathrm{d}Q}{\mathrm{d}z} = 2\alpha M^{1/2} \tag{3}$$

$$\frac{\mathrm{d}}{\mathrm{d}z}\left(\beta_g M\right) = \frac{FQ}{\theta_m M} \tag{4}$$

$$\frac{\mathrm{d}}{\mathrm{d}z}\left(\frac{\theta_g}{\theta_m} F\right) = -N^2 Q \tag{5}$$

$$\frac{\mathrm{d}}{\mathrm{d}z}\left(\gamma_g \frac{M^2}{Q}\right) = 2F + \delta_g \frac{M^{5/2}}{Q^2} \tag{6}$$

Here, N^2 is the buoyancy frequency associated with the ambient fluid and α is the entrainment coefficient, arising from the hypothesis $-\left[ru\right]_{r=\infty} = \alpha r_m w_m$ made by MTT which says that the inward radial volume flux is proportional to the vertical volume flux in the plume. The remaining parameters $\beta, \theta, \delta, \gamma$ are profile coefficients describing the relative shape of the self-similar profiles and are a more modern development. Note that equations (3)–(6) are consistent with both top-hat and Gaussian radial profiles, but inconsistent with the MTT assumption that profiles of different variables share the same width.

The above theory provides a basis for examining simulations of turbulent plumes. The PhD thesis of Craske (2016) and associated papers (e.g. van Reeuwijk et al. (2016), henceforth VR16) consider direct numerical simulation of a turbulent jet, forced plume and pure plume in a 3D domain with open boundaries and a homogeneous environment. They use the integral theory of MTT, with the turbulent corrections provided by profile coefficients, to examine the turbulent dynamics and entrainment properties in each flow. Following their work, we process the results of numerical simulations by performing an azimuthal average to separate the mean and turbulent components. Note that in theory, these averages are over the semi-infinite domain $r > 0$ but clearly a simulation has a finite domain. We minimise the error associated with finite domain approximations of integrals over an infinite radial domain via 'thresholding', which places the upper limit of the integral at the first point where the vertical velocity reaches a small fraction of its value on the centreline.

2.2 Simulation methods

Numerical simulation of the plume penetration problem offers some potential advantages over laboratory experiments; for instance, it is straightforward to include complicating factors such as large-scale horizontal flow, or simple representations of physical effects, as well as providing access to full 3D dynamical fields which may be used for analysing the flow. For this work, we use the Fortran codebase 'DIABLO'. DIABLO evolves a discrete approximation of the Navier-Stokes equations (7), (8) and buoyancy evolution equation (9) using a pseudo-spectral method in the horizontal with periodic boundary conditions and finite difference in the vertical with fixed wall boundaries. Owing to the large range of scales in the UTLS, resolving turbulent scales with direct numerical simulation would incur a great computational cost. We therefore use large eddy simulation (LES) with the anisotropic minimum dissipation (AMD) eddy-viscosity model for capturing the dynamic effects of unresolved scales (Vreugdenhil and Taylor, 2018). The dimensional governing equations are

$$\frac{\partial \widehat{u}_i}{\partial x_i} = 0 \tag{7}$$

$$\frac{\mathrm{D}\widehat{u}_i}{\mathrm{D}t} + \frac{\partial \widehat{p}}{\partial x_i} = \nu \frac{\partial^2 \widehat{u}_i}{\partial x_j \partial x_j} + \widehat{b}\delta_{i3} - \frac{\partial \tau_{ij}}{\partial x_j} \tag{8}$$

$$\frac{\mathrm{D}\widehat{b}}{\mathrm{D}t} = \kappa_b \frac{\partial^2 \widehat{b}}{\partial x_j \partial x_j} - \frac{\partial \lambda_j}{\partial x_j} \tag{9}$$

where $\widehat{\cdot}$ indicates filtering at the resolved grid scale, δ_{ij} is the delta function, ν is the kinematic viscosity, κ_b is the diffusivity of buoyancy $b = -g\rho'/\rho_0$, the sub-grid-scale (SGS) stress is $\tau_{ij} = \widehat{u_i u_j} - \widehat{u}_i \widehat{u}_j$ and the SGS buoyancy flux is $\lambda_j = \widehat{u_i b} - \widehat{u}_i \widehat{b}$. The eddy-viscosity model for the deviatoric component of the SGS stress and the SGS buoyancy flux are

$$\tau^d_{ij} = \tau_{ij} - \frac{1}{3}\delta_{ij}\tau_{kk} = -2\nu_T \widehat{S}_{ij}, \qquad \lambda_j = -\kappa_{b,T} \frac{\partial \widehat{b}}{\partial x_j} \tag{10}$$

where ν_T and $\kappa_{b,T}$ are the turbulent eddy viscosity and eddy diffusivity respectively, each determined by the AMD scheme. The hat notation is now dropped for convenience.

For simulating plumes, we may non-dimensionalise via the source radius r_0 and the integral source buoyancy flux $F_0 = r_0^2 w_0 b_0$ with $[F_0] = L^4 T^{-3}$, leaving two characteristic numbers $\mathrm{Re} \equiv (F_0 r_0^2)^{1/3}/\nu$ and $\mathrm{Pr} \equiv \nu/\kappa$. The intrinsic velocity scale is $U \sim F_0^{1/3} r_0^{-1/3}$ and the intrinsic timescale is $T \sim r_0^{4/3} F_0^{-1/3} \equiv r_0/U$ known as the *turnover time*, interpreted as the time for an eddy to become significantly distorted (Frisch, 1995). In this initial verification work, the background buoyancy profile is unstratified for simplicity, but later we impose a linear stratification on the background profile. A buoyant plume is generated using a volumetric forcing method in which the buoyancy and vertical velocity are relaxed towards prescribed analytic profiles for a pure plume, derived from the MTT equations (3)–(5), in a thin region at the bottom of the domain. A random 10% perturbation is applied to the profile in the forcing region and to the velocity in the two grid layers above the forcing region to initiate turbulence. The forcing region is set by two parameters L_c and L_p which control a tanh function modulating the prescribed profiles. To illustrate, given vertical profiles $r_m(z), b_m(z)$ consistent with the desired plume, the

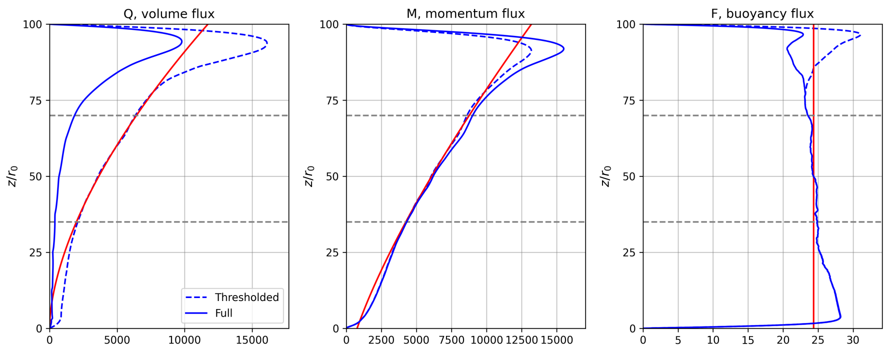

Figure 1: Variation of integral quantities Q, M, F defined by (2) with height z. Results from simulation described in section 2.2 with w-based thresholding shown in dashed blue and the original (full) integral quantities shown in blue. MTT analytic predictions fitted to the simulation data shown in red. Dashed grey lines indicate the region used to fit the analytic curves.

forcing applied to b (excluding random perturbations) is

$$f_b(\boldsymbol{x}) = \left(b(\boldsymbol{x}) - 2b_m(z)\exp\left[-\frac{1}{2}\frac{x^2+y^2}{r_m(z)^2}\right]\right)\left(\frac{1}{2} - \frac{1}{2}\tanh\left(\frac{z-L_c}{L_p}\right)\right) \tag{11}$$

The first factor is the difference between the dynamical buoyancy field and the prescribed buoyancy (assuming a Gaussian radial profile), whilst the second factor limits the forcing to $0 \leq z \lessapprox L_c + L_p$. The parameter L_c approximately controls the depth of the forcing region and L_p determines how sharply the forcing decays above $z = L_c$. The forcing region is indicated in figure 2 and in the schematic in figure 7 of the stratified setup used later. A parameter $1/\tau$ controls the coupling strength with the momentum equations. The size of τ is arbitrary other than being small enough to control against dynamical variation and large enough to prevent numerical instability.

In the remainder of this section, all data is from a high resolution LES simulation with grid size $N_x \times N_y \times N_z = 1024 \times 1024 \times 1025$, dimensional size $L_x = L_y = \frac{1}{2}L_z = 50r_0$, source radius $r_0 = 10\,\mathrm{m}$ and source buoyancy flux $F_0 = 0.08r_0^2\,m^4 s^{-3}$. For the unstratified plume, simulations are first run until the plume is fully developed and 'statistically steady', which is verified by ensuring buoyancy and vertical velocity exhibit self-similar profiles and the running time average with n timesteps of each variable is sufficiently steady. The number of observations n must be large enough that the total time over which samples are averaged is greater than the intrinsic timescale T of the flow. The simulation is then run in data-collection mode for approximately 100 turnover times. For a discussion of the azimuthal averaging & Reynolds' decomposition method and limitations of this simulation setup, see appendix A and B respectively.

2.3 Integral quantities, self-similarity and entrainment

In the integral formulation, the plume dynamics are fully determined by r_m, w_m and b_m, which in turn are fully determined by the vertical evolution of integral quantities Q, M and F. Figure 1 shows the variation of these quantities with height (streamwise distance) z. Following the methods of Craske (2016), we calculate infinite radial integrals by thresholding the domain at the radius where vertical velocity $\overline{w}$ falls below a specified ratio ε of the centreline vertical velocity. The thresholded data is of particular interest as it represents the fluxes contained within the plume, excluding the surrounding environment. The integral formulation of the plume equations (3)–(5) admit power-law solutions with scalings $Q \sim z^{5/3}, M \sim z^{4/3}$ and $F \sim$ const. Curves of this form are shown in figure 1 and demonstrate a good fit with the thresholded integral fluxes.

Figure 2 shows the azimuthally averaged vertical velocity and buoyancy fields. The buoyant plume appears as a region of strong vertical velocity localised to small radii. The linear increase of plume radius with height as predicted by MTT theory is evident. The dashed black line shows the analytic radius r_m (calculated from the power-law solutions for M and Q) as a function of

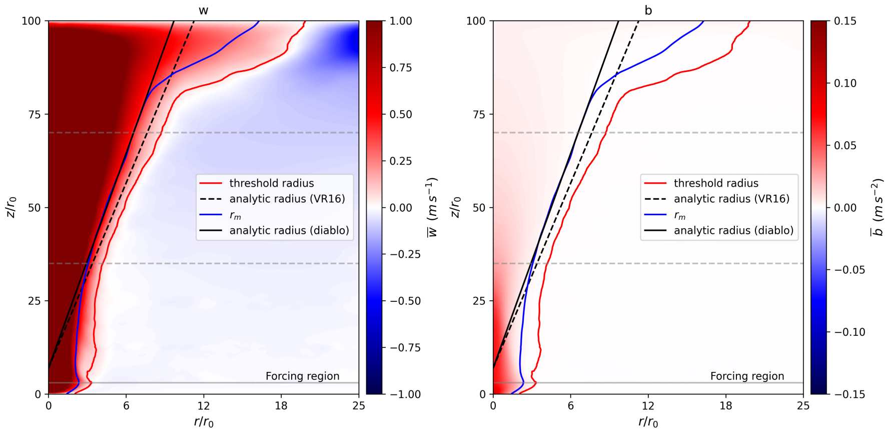

Figure 2: Azimuthally & ensemble averaged vertical velocity w (left) and buoyancy b (right). Variation of characteristic plume radius $r_m(z)$, analytic radius from DIABLO simulations, analytic radius from VR16 simulations, and threshold radius used for computing radial integrals are overlaid.

height using the value of the entrainment coefficient found in VR16 direct numerical simulations, $\alpha = 0.105$. The solid black line uses the entrainment coefficient resulting from our large eddy simulations, $\alpha = 0.09$, which demonstrates slightly weaker entrainment in our simulations, but still within the range of α found in the literature. Figure 2 also demonstrates that only the middle third of the domain is suitable for analysis; the forcing region at the bottom of the domain, in which the vertical velocity and buoyancy are forced, underlies an adjustment region in the bottom third of the domain where source effects gradually decay. In the top third of the domain where the plume impinges on the closed top boundary and spreads laterally, a weak stratification is gradually introduced which inhibits the rise of the plume.

Self-similarity is one of the central ideas of MTT theory. The vertical velocity, buoyancy, radial momentum and buoyancy flux profiles over a range of streamwise heights z are shown normalised by the characteristic scales r_m, b_m, w_m at each height in figure 3, demonstrating convergence to a single radial profile. This is a useful diagnostic for future simulations; self-similar profiles indicate that the plume is fully developed. Figure 3 also shows the normalised radial velocity and specific volume flux. Whilst they are approximately self-similar, there is more spread than the $\overline{w}, \overline{b}$-profiles, likely due to the periodic (i.e. effectively closed) boundaries as compared with the open boundaries of VR16. In our case, the periodic boundaries result in an overturning circulation which disrupts the radial outflow from the plume. Nonetheless, the radial specific volume flux tends towards $-\alpha$ as r/r_m increases which verifies the entrainment hypothesis and demonstrates that plume entrainment is behaving broadly as expected.

Figure 4 shows the vertical evolution of the entrainment coefficient, calculated directly from the MTT equations which give $\alpha = (2M^{1/2})^{-1} dQ/dz$. The value calculated from a linear fit of the characteristic plume radius r_m to z is shown by a black vertical line α_p. Whilst there is significant variation, in the middle third of the domain suitable for analysis α lies within a narrower band $0.06 < \alpha < 0.1$, again within the range found in the literature. The flux balance parameter Γ is also shown in figure 4. This is a normalised Richardson number, defined as

$$\Gamma = \frac{5FQ^2}{8\alpha_p \beta_g \theta_m M^{5/2}} \tag{12}$$

indicating the balance of gravitational and inertial forcing. A 'pure' plume has $\Gamma = 1$, a 'lazy' plume $\Gamma > 1$, a 'forced' plume $0 < \Gamma < 1$ and a jet has $\Gamma = 0$. In our simulations, away from the source $\Gamma \approx 0.5$ indicating a forced plume in which buoyancy dominates, but with inertial forcing present. Whilst our simulations use forcing conditions for a pure plume, it is clear from

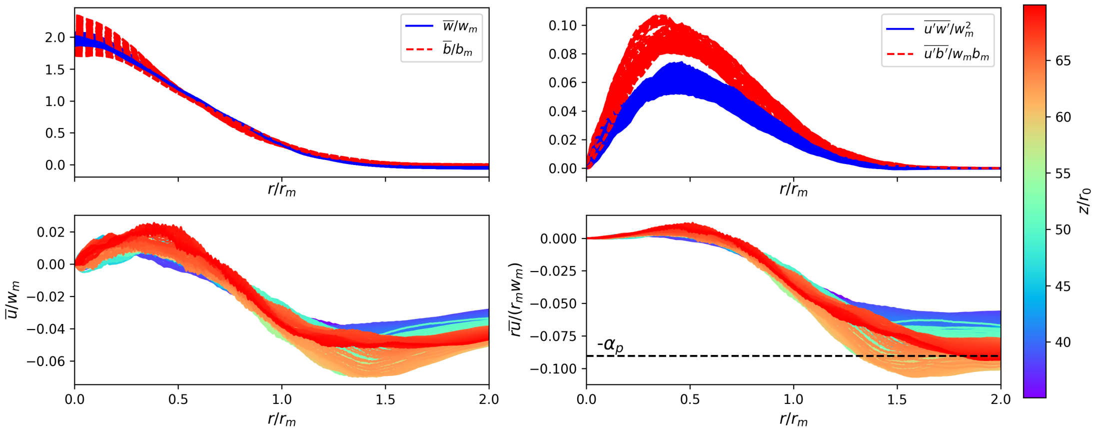

Figure 3: Self-similar radial profiles of $\overline{w}, \overline{b}$ (top left), radial momentum and buoyancy fluxes $\overline{u'w'}$ and $\overline{u'b'}$ (top right), mean radial velocity $\overline{u}$ (bottom left) and normalised mean radial specific volume flux $r\overline{u}$ (bottom right) in the interval $35 < z/r_0 < 70$. Dotted line indicates value of α_p calculated from a linear fit of r_m and z.

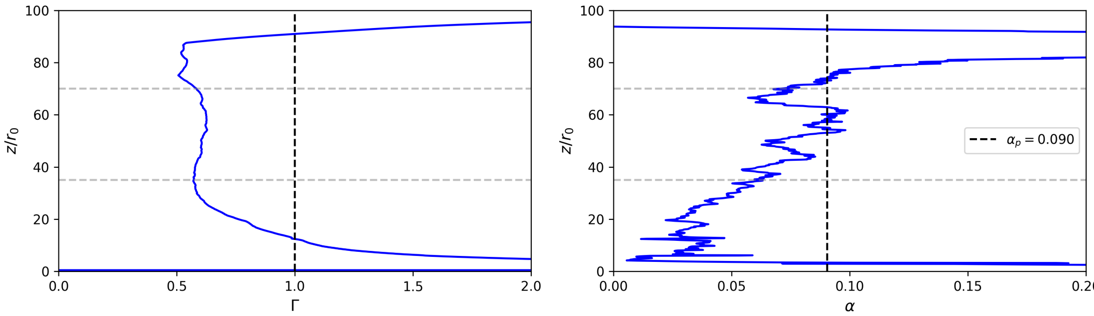

Figure 4: Vertical evolution of the flux balance parameter Γ (left) and the entrainment coefficient $\alpha = (2M^{1/2})^{-1}\mathrm{d}_z Q$ (right).

comparison with VR16 that our results more closely match those of a forced plume, since our volumetric forcing method involves relaxing the vertical velocity which introduces some inertial forcing. This illustrates the difficulty of balancing the inertial and buoyancy forcing to obtain a pure plume, which is often cited as a reason for simulating forced plumes or jets instead. Since pure plumes and jets are special cases where Γ takes a single value, a forced plume can be considered the more general case. We anticipate that a forced plume is therefore more representative of the atmospheric case.

2.4 Profile coefficients and turbulence characteristics

Profile coefficients are a modern addendum to the MTT plume equations which, in a radially averaged sense, account for the (non-dimensionalised) eddy terms neglected when radially integrating the Boussinesq equations and act to modify the shape of self-similar profiles for each variable (Craske and van Reeuwijk, 2015). In a fully developed self-similar plume, the coefficients are constant, which provides another check on development of the plume in future simulations. The coefficients β, θ, δ and γ are associated with the dimensionless momentum flux, buoyancy flux, turbulence and energy flux respectively. The subscripts m, f and p refer to contributions from the mean flow, turbulence, and pressure respectively. The vertical variation of these contributions are shown in figure 5. The mean flow and turbulence contributions are roughly constant in the analysis region, and match the values found in VR16. The pressure contribution varies with height, likely due to the partly-closed nature of the domain and the associated overturning circulation

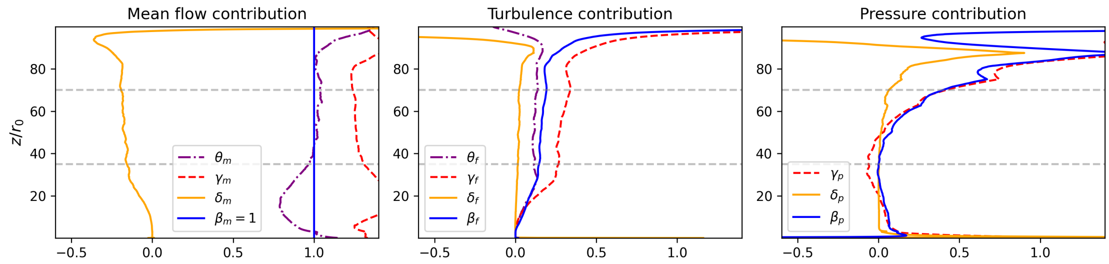

Figure 5: Vertical evolution of mean profile coefficients for mean flow, turbulence and pressure contributions.

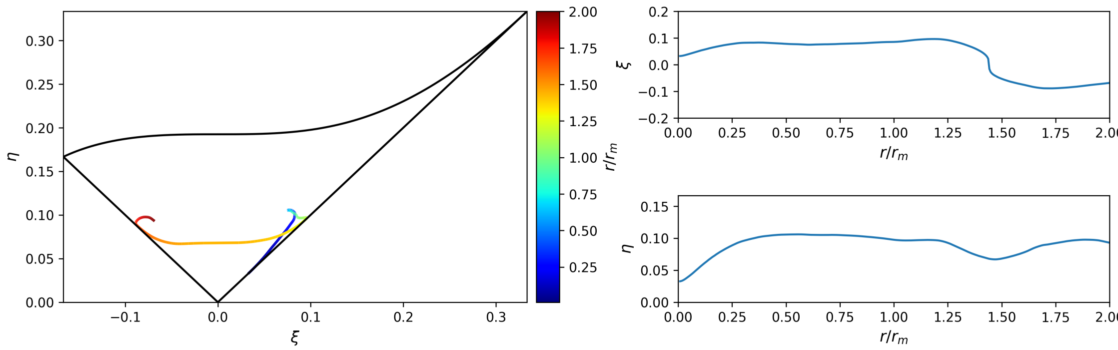

Figure 6: Invariants of the anisotropy tensor (13), plotted in (ξ, η) space with the Lumley triangle (left), dependence of ξ, η on r/r_m (right).

discussed earlier, which reduces pressure at the bottom of the domain and increases pressure at the top.

The characteristics of turbulence in the plume may be explored in two ways. Anistropy is investigated by considering the invariants of the deviatoric component of the Reynolds stress tensor, known as the anistropy tensor b_{ij} and defined as

$$b_{ij} = \frac{\overline{u_i' u_j'}}{\overline{u_i' u_i'}} - \frac{1}{3}\delta_{ij} \tag{13}$$

where $\bar{\cdot}$ is the mean component of an appropriate Reynolds' decomposition. The first invariant $\mathrm{Tr}(\boldsymbol{b})$ is zero and following Lumley and Newman (1977), the second and third invariants η, ξ are defined as $6\eta^2 = b_{ij}b_{ji} = \mathrm{Tr}(\boldsymbol{b}^2)$ and $6\xi^3 = b_{ij}b_{jk}b_{ki} = \mathrm{Tr}(\boldsymbol{b}^2)$. These variables describe any physical state of turbulence in a 2D map known as the 'Lumley triangle'. The second invariant $\eta > 0$ identifies the degree of anistropy in the flow field, where large η indicates strong anisotropy. The third invariant ξ determines if the turbulence state is one-component, two-component, axisymmetric, etc. In the plume, we expect weak anistropy (small η) and axisymmetric turbulence, indicated by $\xi = \pm\eta$. This is indeed found in the results as shown in figure 6 and there is remarkable similarity with the same results presented in VR16.

3 Convective penetration into a stably stratified layer

With the capability for DIABLO to reliably simulate plumes verified and the essential behaviour of a buoyant plume established, we move closer to the atmospheric case by introducing a stably stratified layer and a passive tracer carried by the plume. We will explore the dynamics in this stratified case which exhibits the formation of a 'fountain' and a radially spreading intrusion, and compare our results with similar laboratory experiments in the literature.

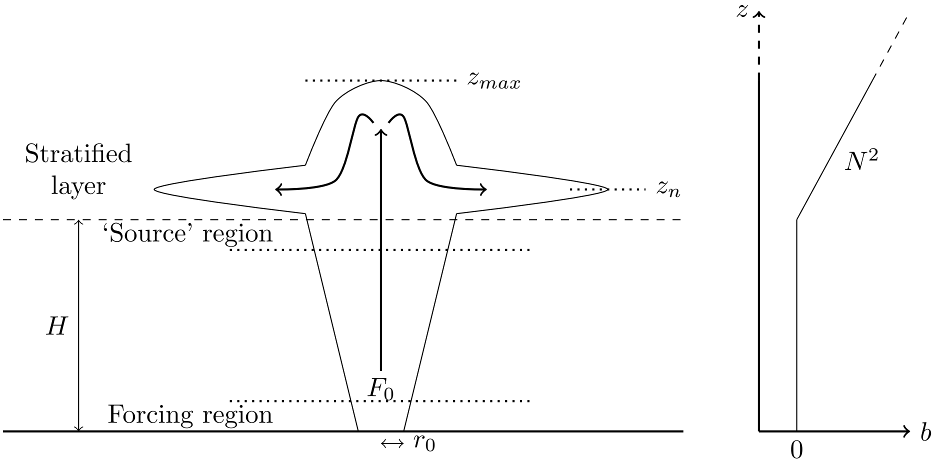

Figure 7: Simulation setup and key quantities & regions for convective penetration of a buoyant plume into a stratified layer.

3.1 Simulation configuration and results

Figure 7 shows a schematic of the simulation setup with an unstratified region of depth H at the bottom of the domain and a stably stratified region in the remainder of the domain with constant buoyancy frequency N^2. We use the same plume generation method as in the fully unstratified domain, with a source radius r_0 and source buoyancy flux F_0. A sponge layer is added in the top 20% of the domain, where the velocity is damped to remove the reflection of internal gravity waves from the top boundary. For the purposes of verifying initial simulation results, the values of the parameters r_0, H, N^2 and F_0 are computed from the experimental setup used in laboratory experiments by Ansong and Sutherland (2010). Note that throughout this essay, we will describe the simulations using physical scales that correspond to the laboratory context, e.g. the vertical co-ordinate z often uses centimetres. However, rescaling of these quantities is possible, to make the results relevant to the atmospheric case.

To aid in the examination of the flow evolution and mixing, we include a passive tracer ϕ satisfying the same dynamical equation as buoyancy. The tracer – an arbitrary scalar – is passive in the sense that it has no coupling with the momentum equation so does not influence the dynamics, it simply follows the flow. The field ϕ represents the tracer concentration, which diffuses according to an associated diffusivity κ_ϕ which for convenience is the same as the diffusivity of buoyancy here but may differ in general, as well as a turbulent (or eddy) diffusivity $\kappa_{\phi,T}$. The turbulent diffusivity is computed by the LES model and accounts for sub-grid scale diffusion. This may locally exceed the prescribed diffusivity by several orders of magnitude. The tracer is forced using the same volumetric method as the buoyancy, giving a constant source of tracer with a Gaussian radial profile in the forcing region. Note that regardless of the forcing profile, turbulent mixing in the plume results in the azimuthally averaged tracer concentration having a Gaussian profile far from the source.

Figure 8 shows the tracer concentration within white contours and the wave field $\partial_t N^2$ outside, visualising the flow evolution which proceeds as follows. Initial penetration of the plume cap results in generation of internal gravity waves over a range of frequencies, and without subsiding fluid the plume reaches its maximum penetration height (figure 8(a)) around $t \sim 6s$. At this stage, internal gravity waves are beginning to propagate away from the plume cap. As the plume pushes into the stratified layer, the relative buoyancy becomes negative and the plume fluid overturns and subsides. At $t \sim 8s$, further internal gravity waves are produced, now in a more regular pattern, with similar amplitude to the initial waves (figure 8(b)). The subsiding fluid falls to its level of neutral buoyancy and spreads as an intrusion (figure 8(c)). At $t \sim 15s$ the waves cover the entire region above the spreading current and appear to have a narrow frequency band (i.e. most waves at the same angle). Furthermore, the highest amplitude waves can be traced back to

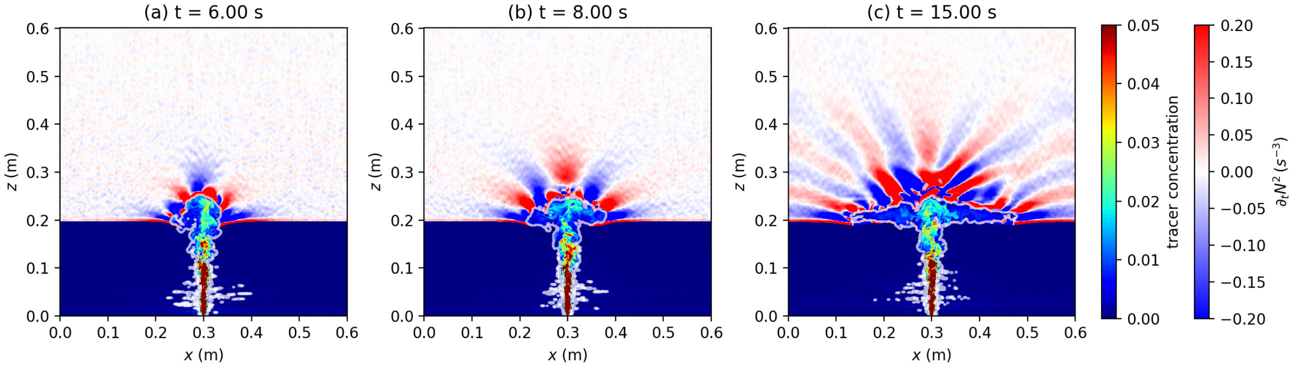

Figure 8: Stages of buoyant plume penetration into a stratified layer at $z = 0.2\,\mathrm{m}$. Passive tracer field shown inside white contour, wave field representation $\partial_t N^2$ shown outside white contour. Note that Gibbs ringing artefacts are visible in the lower part of the domain. Simulation with $H = 20\,\mathrm{cm}, r_0 = 0.2\,\mathrm{cm}, F_0 = 0.15r_0^2\,\mathrm{m}^4\mathrm{s}^{-3}$ and $N = 1.75\,s^{-1}$.

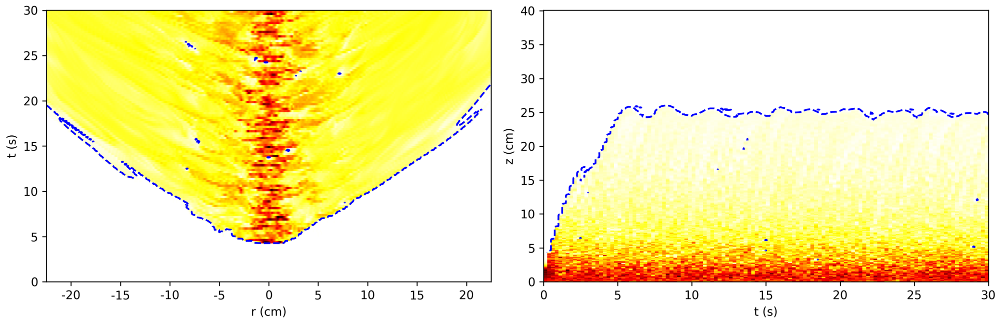

Figure 9: Horizontal (left) and vertical (right) time series of the same simulation shown in figure 8. The horizontal time series is formed of slices taken at the neutral buoyancy level $z \approx 20.9\,\mathrm{cm}$ and the vertical time series is formed of slices through the plume centreline. Colour represents the tracer concentration and the blue dashed line indicates the tracer contour used for calculations.

the oscillating plume cap, with some additional waves produced by the spreading intrusion. These results match qualitatively with studies in the literature, e.g. Ansong and Sutherland (2010); Hunt and Burridge (2015); Devenish et al. (2010).

3.2 Comparison with lab experiments

To demonstrate quantitative agreement between our simulations and similar studies in the literature, we perform analyses of the maximum penetration height $z_{\max}$, neutral buoyancy height z_n and intrusion spreading rate V_r. These quantities are computed by considering horizontal and vertical time series through the plume centreline; see figure 9 which emulates the experimental method used by Ansong and Sutherland (2010), henceforth AS10. The left-hand panel shows horizontal slices of the tracer field taken at the level of neutral buoyancy (calculation discussed in the next subsection) and through the plume centreline, showing the intrusion spreading radially. The right-hand panel shows vertical slices of the tracer field through the plume centreline, showing the plume penetrating into the stratified layer at $H = 20\,\mathrm{cm}$, reaching its maximum height $z_{\max}$ then oscillating about the quasi-steady-state height z_{ss}. Note that whilst AS10 perform experiments with $H = 0, 5, 10, 15\,\mathrm{cm}$, as discussed in appendix B, we are limited to larger values of H so that the plume may become fully developed. We consider simulations with $H = 10, 15, 20\,\mathrm{cm}$ and $r_0 = 0.2\,\mathrm{cm}, F_0 = 0.15r_0^2\,\mathrm{m}^4\mathrm{s}^{-3}, N = 1.75\,s^{-1}$ in figure 10.

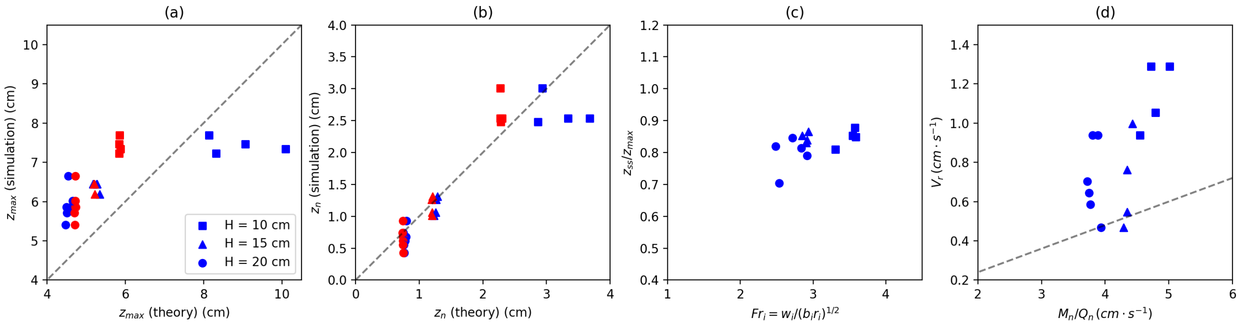

Figure 10: Comparisons of (a) maximum penetration height and (b) neutral buoyancy height between simulation and theory; (c) quasi-steady-state height versus interfacial Froude number; (d) radial intrusion spreading rate versus ratio of momentum and volume fluxes. In (a) and (b), the AS10 numerical method is shown in blue, and the simplistic approximation detailed in section 3.3 is shown in red.

Qualitatively, the results matches those of AS10, with the maximum penetration height remaining well above the bottom of the stratified layer and the neutral buoyancy height slightly above, as expected from the simulation parameters. In particular, figure 10(a) and (b) show that for $H = 10, 15, 20\,\mathrm{cm}$ we find a similar range of maximum penetration heights and neutral buoyancy heights. Note that we find fewer values of $z_n < 0.5\,\mathrm{cm}$ in our simulations; this discrepancy could be attributed to the fact we can precisely generate a linear stratification profile with fixed N^2 in the simulations, but this is not necessarily the case in the lab. The generally worse predictions for the $H = 10\,\mathrm{cm}$ case suggest the unstratified layer is not deep enough for the plume to become fully developed. There are two other differences present when comparing our data with AS10. Figure 10 (c) shows the ratio of the quasi-steady-state height z_{ss} and $z_{\max}$ versus the interfacial Froude number

$$\mathrm{Fr}_i = \frac{\overline{w}_i}{\left(\overline{b}_i \overline{r}_i\right)^{1/2}} \tag{14}$$

where the overbar represents a temporal average over the entire simulation post-penetration, as well as a spatial average over the width of the plume, and subscript i represents the value at the interface. In our simulations, we find a much smaller range of $z_{ss}/z_{\max}$ compared to that in AS10, though we also sample a smaller range of interfacial Froude numbers. However, in agreement with AS10, no particular correlation between Fr_i and $z_{ss}/z_{\max}$ is found. Similarly, no correlation is found between H and Fr_i, as one may expect, since for an unstratified plume in the lower region $w_i \sim H^{-1/3}$, $b_i \sim H^{-5/3}$, $r_i \sim H$ according to the MTT analytic solution of (3)–(5), hence $\mathrm{Fr}_i \sim 1$. For the case of a fountain in a linearly stratified environment, Bloomfield and Kerr (1998) found an average $z_{ss}/z_{\max} \approx 0.93$. Figure 10 (d) shows the radial intrusion spreading rate V_r in the simulations versus the ratio of momentum flux to volume flux at the neutral buoyancy height M_n/Q_n. AS10 find a relationship of the form

$$V_r = (0.12 \pm 0.02)\frac{M_n}{Q_n} \tag{15}$$

which is plotted as a dashed grey line in figure 10. Evidently our simulation results do not match this relationship, though a small range of M_n/Q_n is sampled. Nonetheless, we find the range of spreading rates V_r broadly matches the range found in AS10, and we find a similar range of M_n/Q_n compared with AS10 for the sampled values of H. Together, these results demonstrate that our simulations of a plume penetrating a stably stratified layer are reliably capturing the dynamics seen in laboratory experiments of the same setup.

3.3 Estimates of maximum penetration height

The maximum penetration height is of central importance in this problem, as it determines the maximum level of fluid detrainment (Ansong et al., 2008) and in the atmospheric case, it is directly linked to temperature constraints on the concentration of water vapour (Jensen et al., 2007). The TTL contains the 'cold-point tropopause' defined as the minimum of the temperature profile (Fueglistaler et al., 2009); if the maximum penetration height of a convective overshoot exceeds this altitude and reaches larger temperatures, then the water vapour transported to this altitude is more likely to remain in the stratosphere as greater potential temperatures are accessed. Furthermore, as the environmental temperature increases, the sublimation of ice hydrometeors is aided. This process is critical to determining whether a convective overshoot ultimately hydrates the stratosphere (Dauhut et al., 2018).

AS10 compute predictions of $z_{\max}$ and z_n using a numerical method whereby the MTT plume equations are numerically solved using values of M, F and Q evaluated at the interface $z = H$ as initial conditions. In this method, $z_{\max}$ is defined as the point where the momentum flux M vanishes, and the neutral buoyancy height is where the buoyancy flux F vanishes. Application of the same method to our simulation data is shown in figures 10(a) and (b). The grey vertical lines indicate the interfacial values of M, F and Q used as initial conditions. The neutral buoyancy height is well predicted, as was found in AS10. The maximum penetration height is generally underpredicted by this method, with values on average 80% of the true value. Examining the numerical solutions for M, F and Q compared to the actual fluxes in figure 11 shows that the reasonable agreement found is perhaps surprising, as the numerically solved flux profiles do not resemble the simulated fluxes. M is perhaps the closest representation, but F and Q do not represent the data well and as the three variables are coupled, the efficacy of this technique could be questioned. This itself is not unsurprising: the MTT equations as applied assume there is no mixing of ambient fluid between the neutral level and the maximum height, which would raise the maximum height if accounted for, as plume fluid entrains positively buoyant fluid. In any case, the MTT assumption that entrainment is proportional to axial velocity breaks down once the plume becomes a fountain in the stratified region, so equations (3)–(5) should not be applicable. Note that figure 11 shows the *full* fluxes, calculated over the entire domain, and the *thresholded* fluxes, representative of the flux inside the plume (or the rising component of the fountain) itself. Whilst one might expect the thresholded flux within the plume would yield the best estimate, this is the case for z_n but using the full fluxes as initial conditions produces the best estimates for $z_{\max}$ as demonstrated in the figure. Further corrections may be applied to the MTT equations to refine this technique, for example the 'unaltered volume flux' method, which numerically solves F and M using the unstratified Q-profile. Devenish et al. (2010) use this technique to argue that the reasonable agreement found with z_n suggests that stratification does not play a significant role below the neutral buoyancy height.

More simplistic methods may be used to estimate $z_{\max}$ and z_n. In some cases, non-dimensionalised numerical solutions of the MTT equations can be fitted to LES data, e.g. Devenish et al. (2010). The maximum penetration height may also be estimated via a simplistic energetic argument: the kinetic energy density at penetration, $E_k(H)$, and potential energy density at height z, $E_p(z)$, on the centreline are

$$E_k(H) = \frac{1}{2}\rho(2w_m)^2 = \frac{1}{2}\rho\left[4\cdot\left(\frac{5}{6\alpha}\right)^2\left(\frac{9}{10}\frac{\alpha}{\theta_m\beta_g}F_0\right)^{2/3}H^{-2/3}\right] \tag{16}$$

$$E_p(z) = \frac{1}{2}\rho N^2(z-H)^2 \tag{17}$$

Neglecting dissipation and assuming that all KE is converted to PE at $z = z_{\max}$, we find

$$z_{\max} = \frac{2}{N}\left(\frac{5}{6\alpha}\right)\left(\frac{9}{10}\frac{\alpha F_0}{\theta_m\beta_g}\right)^{1/3}(H-z_v)^{-1/3} \sim \alpha^{-2/3}F_0^{1/3}H^{-1/3}N^{-1} \tag{18}$$

A similarly simplistic argument for the neutral buoyancy height assumes that without mixing, fluid will come to rest at the level with the same environmental buoyancy as the average plume

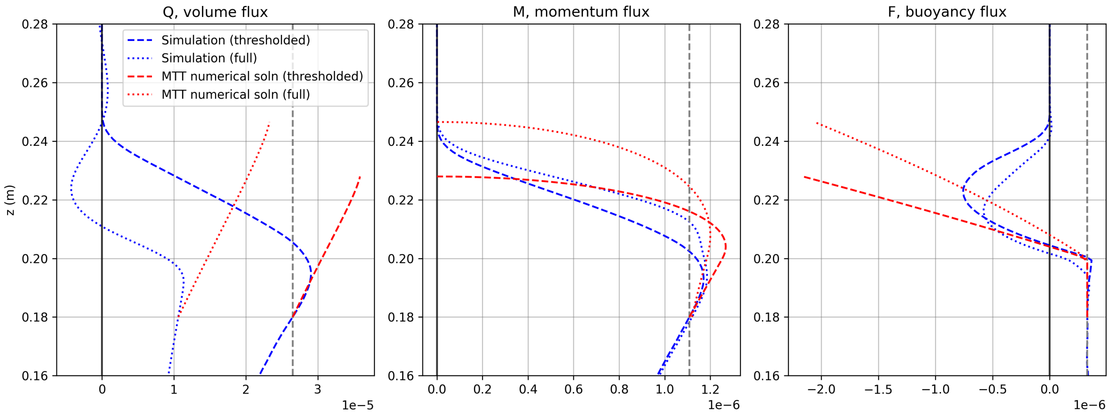

Figure 11: Vertical profiles of volume, momentum and buoyancy flux within the plume (thresholded) and across the entire domain (full). Blue lines indicate the profiles computed from simulations in DIABLO, red lines indicate profiles from numerically solving the MTT plume equations (3)–(5) with initial conditions taken from simulation results at the bottom of the stratified layer. Data from the same simulation as figure 8.

buoyancy at penetration $\overline{b}_i = 2b_m(H)$. Hence, the neutral buoyancy height is approximately

$$z_n = \frac{5F_0}{3\alpha\theta_m N^2}\left(\frac{9}{10}\frac{\alpha}{\beta_g\theta_m}F_0\right)^{-1/3}(H-z_v)^{-5/3} \sim \alpha^{-4/3}F_0^{2/3}H^{-5/3}N^{-2} \tag{19}$$

Figure 10 shows these estimates for each simulation in red, compared with the AS10 method in blue. The same relationships are seen; $z_{\max}$ is underpredicted whilst z_n is reasonably well predicted, illustrating in this case that simplistic methods sometimes exhibit the same predictive value as more complex methods.

In the atmospheric case, there are many complications which play a role in setting the penetration depth of a convective plume. For example, latent heating in the rising plume effectively increases the buoyancy flux at penetration. This can be accounted for in simulations (which neglect latent heat) by increasing the source buoyancy flux. As a further example of the complexity, Tailleux and Grandpeix (2004) discuss the need for a correction to the concept of Convective Available Potential Energy (CAPE), computed from the work done by a fluid parcel relative to an environmental sounding up to the level of neutral buoyancy, assuming undiluted ascent. This overestimates the energy available for converting to KE, and therefore the penetration depth, for two reasons: the mass of the condensed water retained during adiabatic ascent, and the negative work due to subsidence of the central updraft. Even in the idealised fluid problem considered thus far, the ideas behind these concepts could be incorporated, for example by subtracting the work done against the subsiding component of the fountain from the KE available for converting to PE, yielding a prediction for the quasi-steady-state height.

Whilst important, estimating the maximum penetration height does not solely answer the questions posed for this problem; $z_{\max}$ determines the maximum *accessible* environmental buoyancy, but the level at which mixing occurs, and the buoyancy of the plume fluid which most efficiently mixes with the environment, determines the final buoyancy of the mixed fluid and therefore whether tracer remains in the stratified layer. Nonetheless, the value of the environmental buoyancy at height $z_{\max}$ offers a useful constraint on the buoyancy of mixed fluid as will be demonstrated in section 4.3.

3.4 Internal gravity waves

The generation of internal gravity waves, visualised by the field $\partial_t N^2$ in figure 8, is an interesting component of this problem for many reasons, though we will only mention it briefly here. Whilst the wave energy flux is a relatively small proportion of the input energy flux by the plume, in the atmospheric case, the dominant wave modes have been shown to modify the immediate cloud environment (Lane and Reeder, 2001), which may facilitate the saturation of stratospheric air surrounding the convective overshoot. Furthermore, gravity waves generated by deep convection play a role in many atmospheric processes; for example, high frequency gravity waves are thought to make a significant contribution to the momentum flux which drives the QBO (Baldwin et al., 2001). Flynn and Sutherland (2004) found the total vertical momentum flux from gravity waves forced by overshooting convection is comparable to topographically forced waves, and since convectively generated waves arise in the UTLS and have non-zero phase speeds, they can propagate upwards and contribute to the gravity wave spectrum driving the QBO. There also remains debate over the dominant wave generation mechanism and the frequency spectrum of the generated waves.

The introduction of shear would allow comparison of the contributions of some of the wave generation mechanisms hypothesised for deep convection. The three leading contenders for this mechanism are: the perturbation of the mean flow caused by the pressure field above a rising convective cell, known as the 'obstacle effect'; the oscillatory deflection of the boundary of the stratified layer, known as the 'mechanical oscillator'; and the 'deep heating effect' as a result of latent heat release (Flynn and Sutherland, 2004). Without a mean flow or latent heating, future work will focus on the mechanical oscillator. We may then establish the energy and momentum flux associated with waves generated by this mechanism, and compare the results with simulations including large-scale shear to compare the contribution from each of the 'obstacle effect' and 'mechanical oscillator' mechanisms.

4 Tracer transport

Having explored the idealised setup with which we approach the atmospheric problem, including understanding the role of key parameters such as $z_{\max}$ and z_n, we move on to considering in detail the passive tracer carried by the plume.

4.1 Tracer distributions in buoyancy coordinates

Mixing is an irreversible process in which the properties of distinct fluid parcels are combined and modified. The blending of properties of fluid parcels which mix is driven by molecular diffusion, which itself is promoted by turbulence. In a stratified flow, the critical property to understand is the buoyancy of a fluid parcel as this will determine its position once any transient dynamics have subsided and the fluid settles and restratifies. The *irreversible* transport of water vapour and other tracers into the stratosphere thus requires fluid parcels carrying tracer to change buoyancy. Therefore, it is of interest to examine the distribution of passive tracer in buoyancy space, where mixing will act to move tracer concentrations to different buoyancies, indicating the diapycnal transport of tracer taking place.

The turbulent mixing of fluid parcels can be considered a two-step process (Davies Wykes and Dalziel, 2014), composed of stirring and diffusion. Stirring geometrically deforms fluid parcels and stretches surfaces of constant buoyancy, increasing the area over which molecular diffusion acts. Moreover, stirring strengthens buoyancy (or scalar) gradients across buoyancy surfaces, further promoting diffusion. Crucially, stirring is – in principle – a reversible process, whilst molecular diffusion is irreversible and we are most interested in the *irreversible* transport of tracer to greater buoyancies. Therefore, a benefit of analysing tracer distributions in buoyancy space is the separation of the effects of stirring and diffusion. Since stirring only deforms fluid parcels, it does not change the tracer concentration or buoyancy within fluid parcels and therefore only the diffusive component of mixing results in changes in the tracer distribution in buoyancy space.

Figure 12 shows a composite over several simulations of the tracer distribution in buoyancy coordinates in the stratified region at multiple times. These distributions are normalised to have unit area, and therefore referred to as a PDF henceforth. Note that the total tracer concentration in the stratified region increases with time (see figure 12 inset), so the unnormalised area under

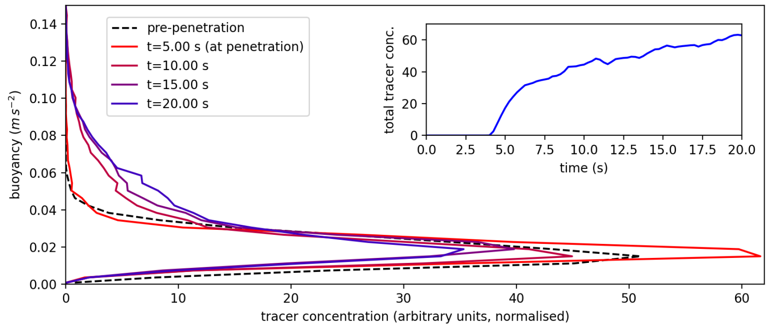

Figure 12: Normalised tracer distribution in buoyancy coordinates in the stratified region indicated in figure 7. Coloured lines are distributions post-penetration at equal time intervals, black dashed line is the time-averaged pre-penetration distribution from the 'source region' indicated in figure 7. Evolution of total tracer concentration (arbitrary units) in the stratified layer inset. Composite of 5 identical simulations (with random perturbations) with $H = 20\,\mathrm{cm}, r_0 = 0.2\,\mathrm{cm}, F_0 = 0.15 r_0^2\,\mathrm{m}^4\mathrm{s}^{-3}$ and $N = 1.75\,s^{-1}$.

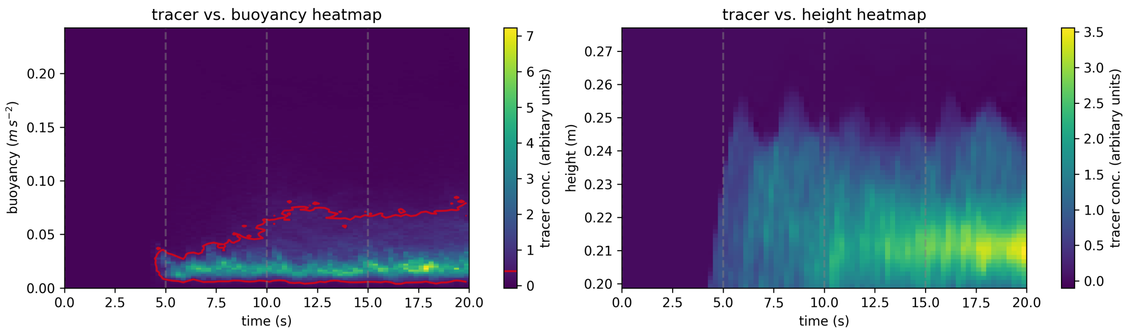

Figure 13: Distribution as described in figure 12, but shown in buoyancy (left) and height (right) coordinates evolving over time. No normalisation is applied to the distributions. Data from simulations with the same parameters as in figure 12.

the curve increases with time. The normalisation therefore allows comparison of tracer distributions at both early and late times by negating this increase in area. A composite is taken to compensate for the random perturbations applied to the forcing profile. A 'source' PDF is taken from a thin layer immediately beneath the stratified layer, referred to as the source region (see schematic in figure 7), which represents the tracer distribution in the plume *before* penetrating the stratified region. Mixing as a result of the penetration process manifests as changes in the PDF. In particular, the mixing of plume fluid containing tracer with more buoyant environmental fluid in the stratified region has two effects, seen as two differences between the black and coloured lines. Fluid parcels with low buoyancies, i.e. those carrying small amounts of tracer at large radii within the plume, immediately encounter more buoyant fluid and mix, giving rise to the decrease in tracer between the source and post-penetration distributions at low buoyancy. Plume fluid that penetrates deep into the stratified region and mixes with much more buoyant environmental fluid produces the increasing 'mass' of the tracer distribution tail at large buoyancies.

Whilst figure 12 is useful for comparing the distribution shape at different times, the dynamical changes and the change in distribution peak are better visualised in a heatmap as shown in figure 13. Moreover, we can also compare the tracer distribution in buoyancy and height coordinates. The horizontal axis shows evolution in time, with colour representing the amount of tracer; in this case, unnormalised, so that the increase in tracer with time is apparent. Nonetheless, we will continue to refer to the distributions as a PDF for convenience. The vertical axes are scaled so that the scales of buoyancy and height coincide, i.e. for the background buoyancy profile, the buoyancy in the left panel corresponds to the height in the right panel. This is verified by noting that at late times, the majority of tracer settles at its neutral buoyancy height, and this level with concentrated tracer in the height and buoyancy heatmaps coincides. Note that the ambient stratification N^2 defines the background buoyancy profile used to link buoyancy and height, but the ambient buoyancy gradient surrounding the plume tends to be weakened by the penetrating plume (note the widening buoyancy contours at the bottom of the stratified layer in the top panels of figure 18), so tracer can reach much larger heights than suggested by the corresponding environmental value of buoyancy. The tracer vs. height view shows the oscillation of the plume around its quasi-steady-state height as well as the collection of tracer in the intrusion. The tracer vs. buoyancy view demonstrates that the distribution at late times is largely similar to that immediately post-penetration at small buoyancies, but there is a significant fraction of tracer that reaches larger buoyancies. However, whilst tracer has reached its maximum height at $t \approx 6\,s$, the presence of tracer at larger buoyancies only becomes evident around $t \approx 10\,s$, indicating that the mixing timescale is perhaps longer (slower) than the dynamical timescale – note the red contour on the left panel at a low tracer threshold, which only reaches buoyancies greater than ~ 0.05 around $t \approx 10\,s$. It also appears that the most 'effective' mixing events, those where there is a notable increase in tracer at larger buoyancies, coincide with larger amounts of tracer being lifted to heights approaching $z_{\max}$, which is likely as a result of the largest eddies (carrying the most tracer) reaching their maximum height.

4.2 Buoyancy-tracer volume distributions

A limitation of the tracer PDF considered thus far is the lack of information on the distribution of tracer at a given buoyancy value; whilst at some buoyancy there may be a peak in the tracer PDF, this may be due to relatively few fluid parcels carrying large tracer concentrations or from relatively many fluid parcels carrying small amounts of tracer; the former results in more effective transport of tracer via mixing. Penney et al. (2020) study mixing by Kelvin-Helmholtz instabilities and use a density-tracer joint PDF to identify irreversible diffusive mixing. For convenience we instead use a buoyancy-tracer volume distribution, i.e. an unnormalised joint PDF. Here, instead of using the (normalised) total tracer concentration of fluid parcels with a given buoyancy as a weight in buoyancy coordinates, we use the total volume of fluid with a given range of buoyancy and tracer as the weight in 2D (b, ϕ) coordinates.

4.2.1 Definition

Formally, we consider a discrete formulation of the probability function following Plumb (2007), with weights $W_{ij}(t)$ evolving in time and the normalisation omitted. We consider the stratified layer as the physical domain, to examine the effects of mixing on tracer and buoyancy in the penetration process rather than in the rising plume. The buoyancy and tracer domains are subdivided into N_b and N_ϕ equally sized bins of size

$$\delta b = \frac{b_{\max} - b_{\min}}{N_b}, \qquad \delta\phi = \frac{\phi_{\max} - \phi_{\min}}{N_\phi} \tag{20}$$

where we choose $b_{\min} = 0$ and $b_{\max} = N^2(L_z - H)$ to capture the smallest and largest environmental buoyancy in the stratified layer, respectively. In cases where the plume does not penetrate a significant distance into the stratified layer, $b_{\max}$ may be reduced to better resolve the volume distribution. Choosing bounds for the tracer domain is more difficult; owing to the turbulent nature of the plume, it is difficult to place an upper limit on the concentration of tracer. We therefore make a rough estimate, using the tracer concentration on the plume centreline at penetration height $z = H$ as predicted by the MTT plume equations:

$$\phi_{\max} = k\frac{5F_0}{3\alpha}\left(\frac{9}{10}\alpha F_0\right)^{-1/3}\left(H + \frac{5r_0}{6\alpha}\right)^{-5/3} \tag{21}$$

where F_0 is the source tracer flux, identical to the buoyancy flux. An additional factor $k > 1$ is included to ensure that random fluctuations of ϕ above this azimuthally averaged approximation are still captured. Tracer concentrations are always positive (or zero) so we choose $\phi_{\min} = 0$.

Denoting the centre of a given bin as (b_i, ϕ_j), the weight is defined as

$$W_{ij}(t) = \sum_V I_{ij}(\boldsymbol{x}, t)\Delta x \Delta y \Delta z \tag{22}$$

where V is the volume of the domain under consideration, Δx_i are the grid-cell widths, and the indicator $I_{ij}(\boldsymbol{x}, t)$ is defined as

$$I_{ij}(\boldsymbol{x}, t) = \begin{cases} 1 & (b(\boldsymbol{x}, t) - b_i, \phi(\boldsymbol{x}, t) - \phi_j) \in \left(-\frac{1}{2}\delta b, \frac{1}{2}\delta b\right] \times \left(-\frac{1}{2}\delta\phi, \frac{1}{2}\delta\phi\right] \\ 0 & \text{otherwise} \end{cases} \tag{23}$$

The weight $W_{ij}(t)$ therefore sums the grid volumes where the buoyancy lies within $\frac{1}{2}\delta b$ of b_i *and* the tracer concentration lies within $\frac{1}{2}\delta\phi$ of ϕ_j.

There are a number of differences between the above formulation and that of Penney et al. (2020). First, we do not normalise the weights $W_{ij}(t)$ by the total volume of the domain V, so that we may modify the weights by subtracting a similarly-defined weight derived from a domain with a different volume, which is needed in section 4.3 for a method for identifying mixed plume and environmental fluid. Note that the normalisation is arbitrary in our context, as we are uninterested in regions with no tracer. We could artificially increase the volume of the domain without modifying the plume, in which case the normalisation factor would change but the distribution and its interpretation would not. The weights therefore form an *unnormalised* joint PDF, and may equivalently be considered as the volume of fluid with buoyancy and tracer concentration close to b_i and ϕ_j, so we refer to this as a volume distribution. Finally, note that plume fluid has non-zero buoyancy by definition, so we wish to exclude fluid parcels with zero buoyancy from the weight. Similarly, to isolate mixed plume and environmental fluid and exclude unmixed ambient fluid, we wish to exclude fluid containing no tracer. Therefore, the intervals used in defining the indicator (23) are open/closed in the opposite sense to Penney et al. (2020); they use intervals of the form $[a, b)$ whilst we use intervals of the form $(a, b]$. The smallest buoyancy and tracer bins are then of the form $(0, \delta b]$ and $(0, \delta\phi]$.

4.2.2 Properties

Buoyancy and passive tracer concentration evolve according to advection-diffusion equations without sources or sinks (outside of the forcing region), which provides a constraint on the evolution of the volume distribution that proves useful when distinguishing pre- and post-mixed fluid. As discussed in Penney et al. (2020), Plumb (2007) and references therein, mixing acts to homogenise the buoyancy and tracer concentration of parcels within a region whose size is determined by the molecular diffusivities κ_b and κ_ϕ. The buoyancy-tracer characteristics of the mixed parcel is then an average of the initial parcels, weighted by their volumes. We therefore have the constraint that after stirring and diffusive mixing, points in buoyancy-tracer space are contained within the convex hull of the initial distribution of buoyancy and tracer. The convex hull is the smallest envelope that contains all non-zero points of the distribution. Since our domain has a buoyancy and tracer input from the plume, in fact at a given time we must consider the convex hull of the current distribution combined with the volume distribution of the fluid arriving into the domain at that time.

A number of useful properties arise from the above constraint, provided the diffusivities of tracer and buoyancy are the same. As the volume distribution continuously evolves, the distribution at the next time step must lie within the convex hull of the current time step. We therefore expect extreme values of buoyancy and tracer to shift towards the mean as a result of mixing. In the absence of a buoyancy or tracer flux, the convex hull must reduce over time and result in a more compact distribution, but this is not the case for convective penetration as we have a continuous influx of buoyancy and tracer into the domain. Nonetheless, for a given range of buoyancy, extreme concentrations of tracer are limited by the cumulative convex hull of the distribution as new plume fluid arrives in the stratified layer, and by mixing with environmental fluid with no tracer, the extrema are eroded. Finally, note that the the convex hull of a line is also a line. Hence if fluid parcels along a line in buoyancy-tracer space mix, they will remain on that line. As a result, fluid

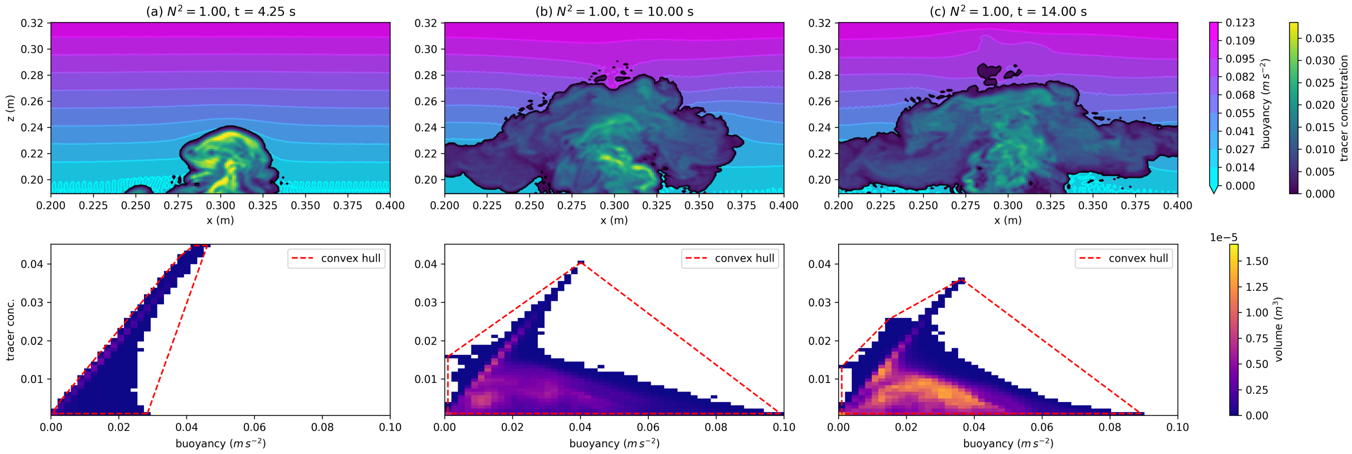

Figure 14: Three instantaneous snapshots of the buoyancy-tracer volume distribution (bottom) with illustrative view of plume tracer field with surrounding environmental buoyancy contours (top). Data from a simulation with $H = 20\,\text{cm}, r_0 = 0.2\,\text{cm}, F_0 = 0.15 r_0^2\,\text{m}^4\text{s}^{-3}$ and $N = 1.0\,s^{-1}$.

on a line in buoyancy-tracer space which has not mixed with fluid parcels elsewhere in buoyancy-tracer space can be distinguished from fluid which *has* mixed, since mixed fluid will no longer be confined to the line.

4.2.3 Results

The volume distribution weights $W_{ij}(t)$ are represented in colour on a 2D plot in figure 14. Three instantaneous snapshots of the distribution are shown with an illustrative view of the plume tracer field and environmental buoyancy contours to demonstrate the associated dynamics. Regions of the volume distribution which are not coloured indicate that no fluid occupies that region of buoyancy-tracer space.

Figure 14(a) shows the volume distribution as the plume first penetrates the stratified layer, with little mixing having taken place. Panel (a) therefore represents the 2D version of the 'source' distribution in figure 12, with a wide variation of tracer over a smaller range of buoyancy in the plume (relative to the stratification). We will discuss the 'source' distribution further in the following subsection. The convex hull shown is that of the distribution at the given time combined with the convex hull of the volume distribution of plume fluid arriving in the stratified layer up to that time. This therefore represents the region in which the current buoyancy-tracer distribution must lie at the next time, though new plume fluid arriving can lie outside this convex hull. Note the small volumes lying outside the previous convex hull in figures 14(b) and (c), which arise from large eddies with strong tracer concentrations entering the stratified layer. In figure 14(b), the effect of mixing becomes clear, as the distribution spreads out from the initial state as plume fluid containing tracer mixes with more buoyant fluid in the stratified region. At late times in figure 14(c), the distribution has not spread much further and the weighting shows that most fluid with non-zero tracer remains at low buoyancies, whilst small amounts of tracer at the edge of the plume mix towards higher buoyancies. It appears that most mixing (i.e. most spreading in the distribution) occurs with intermediate values of tracer, possibly corresponding to the central components of the plume mixing as it overturns near $z_{\max}$. This also indicates that extreme concentrations of tracer entering the stratified layer are homogenised by mixing within the rising plume before mixing with the environment.

The dynamics of the convective penetration process as discussed in section 3.1 are identifiable in the distribution. At initial penetration, large eddies carry significant tracer concentrations up towards $z_{\max}$, with relatively little mixing with the environment on the way up, and some homogenisation within the plume. Panel (a) illustrates this, with a relatively compact distribution and large tracer concentrations. At later times, once the plume cap begins to overturn and significant mixing with the environment occurs near $z_{\max}$, the distribution in panel (b) is more spread out. In particular, we find fluid with low tracer concentrations at large buoyancies, indicating a mixture of plume and environmental fluid. At the particular instant shown in panel (b), there are no large eddies in the plume, and correspondingly the extremes of the tracer concentration arriving in the stratified layer are reduced compared with panel (a). Later still in panel (c), we find significant volumes of fluid appearing at intermediate values of tracer concentration and buoyancy. This is representative of the intrusion forming at the neutral buoyancy height z_n, composed of fluid well-mixed between the environment and plume.

4.3 Distinguishing pre- and post-mixed fluid

The volume distributions shown in figure 14 represent the buoyancy-tracer distribution of *all* tracer-containing fluid in the stratified layer, meaning there is no distinction between plume fluid parcels first arriving in the domain and fluid parcels which have mixed with the environment and had their tracer concentration and buoyancy modified as a result. For the convective penetration problem at hand, it is important to distinguish between these pre- and post-mixed fluid parcels, as the properties of the post-mixed fluid are most relevant to the atmospheric problem. The properties of fluid parcels prior to mixing are simply an idealised representation of convective overshoots arriving in the TTL and are not the focus of the investigation. The key questions relate to how these properties are modified by mixing and how the characteristics of post-mixed fluid depend on the fluid before mixing and other environmental parameters such as stratification strength. We therefore develop a method of distinguishing the pre- and post-mixed fluid by subtracting the volume distribution of fluid *entering* the domain and utilising properties of the volume distribution.

4.3.1 Source line

The idea of using a 'source' distribution to isolate the effects of mixing was exploited in section 4.1 by computing the tracer distribution arriving in the stratified region as a function of buoyancy. Here we apply a similar idea by computing the buoyancy-tracer volume distribution of the plume fluid entering the domain under consideration. Owing to modification of the local buoyancy gradient, the lower fringes of the post-penetration intrusion tends to fall below the original bottom of the stratified layer, $z = H$. Note the widening of buoyancy contours by the spreading intrusion in e.g. figure 14(b), which forces the lower boundary of the stratified layer below its initial height. We therefore modify the domain we consider to $\frac{9}{10}H \leq z \leq L_z$ so that the full plume is captured – we will continue to refer to this as the stratified layer. Formally, we consider a 'cumulative flux' volume distribution with weights $\omega_{ij}(t)$ computed according to

$$\omega_{ij}(t) = \sum_{t^* \leq t} \sum_{V^*} I_{ij}(\boldsymbol{x}|_{z=\frac{9}{10}H}, t^*) w(\boldsymbol{x}|_{z=\frac{9}{10}H}, t^*) \Delta x \Delta y \Delta t^* \tag{24}$$

where I_{ij} is the same as (23) except with $\boldsymbol{x} = (x, y, \frac{9}{10}H)$, and V^* is the 2D surface $z = \frac{9}{10}H$. Each weight $\omega_{ij}(t)$ therefore represents the total volume of fluid with buoyancy and tracer close to b_i, ϕ_j which has entered the stratified layer up to time t.

Figure 16(b) shows the unmodified volume distribution W_{ij} at $t = 15$ s. Figure 16(c) shows the cumulative flux volume distribution ω_{ij} at $t = 15$ s. As expected, the cumulative flux distribution is dominated by inflow. Furthermore, the volume distribution of the arriving plume fluid is a straight line, which follows from MTT plume theory: at a given height, azimuthally averaged radial cross-sections of tracer and buoyancy follow a Gaussian distribution of width r_m, such that

$$\phi(r) = \Phi \exp\left[-\frac{r^2}{2r_m^2}\right] \tag{25}$$

$$b(r) = B \exp\left[-\frac{r^2}{2r_m^2}\right] \tag{26}$$

where Φ and B are constants which may depend on height but not radius. It follows that $\phi \propto b$ at fixed z, such as the bottom of the stratified layer. As a result of the turbulence in the plume we expect a spread around the line, as can be seen in figure 16(c), and furthermore particularly large eddies in the plume may carry buoyancy and tracer values far greater than the mean, though in small volumes – note that small volumes above the source line in the lower panel of figure 14(c) which we mentioned earlier. Examples of this can also be seen in figure 16(b). Owing to the properties discussed in section 4.2.2, since the distribution forms a line, fluid parcels which mix within the rising plume will remain confined to the line. This is a powerful result as it means any fluid parcels appearing elsewhere in the buoyancy-tracer volume distribution *must* have mixed with environmental fluid. Henceforth we will refer to the line appearing in the cumulative flux volume distribution as the 'source line'.

4.3.2 Segregated volume distribution

Given the knowledge that the volume distribution of plume fluid arriving in the domain forms a line regardless of internal mixing as it rises through the stratified layer, we distinguish pre- and post-mixed fluid by identifying whether buoyancy-tracer bins have gained or lost fluid, relative to the distribution arriving in the stratified layer. We refer to this as the segregated volume distribution, with weights $\Omega_{ij} = W_{ij} - \omega_{ij}$. The unmodified volume distribution W_{ij} covers the entire stratified layer whilst the cumulative flux distribution ω_{ij} covers only a single height z, so they refer to different sized volumes; this is the reason for omitting the normalisation used in Penney et al. (2020) and mentioned earlier.

The principle behind the segregated volume distribution can be explained using a schematic of the buoyancy-tracer volume distribution as shown in figure 15. Plume fluid arrives along the blue source line, whilst tracer-less environmental fluid in the stratified layer forms the red line – note this does not appear in W_{ij} (e.g. figure 14) as we exclude tracer-less fluid. If there were no mixing at all, fluid parcels would be unable to modify their buoyancy and tracer concentration so all of the weights Ω_{ij} must vanish. Moreover, if there was no mixing with the environment but the plume could mix internally, all weights away from the source line would vanish. Changes to weights on the (blue) source line would simply indicate the further homogenisation of the volume distribution in the plume from internal mixing, but the line would be preserved. With all turbulent mixing present, as plume fluid mixes with the environment, the volume associated with the source line must decrease and the lost volume will appear elsewhere in the convex hull of the unmixed plume and environmental fluid volume distributions, indicated by the pink region.

The interpretation of the segregated volume distribution is therefore as follows: negative volumes $\Omega_{ij} < 0$ indicate that the total volume of fluid in the stratified layer with those values of buoyancy and tracer has *decreased* after entering the stratified layer and corresponds to plume fluid which has *not* mixed with the environment. Positive volumes $\Omega_{ij} > 0$ indicate that the volume of fluid with those values of buoyancy and tracer has *increased* in the stratified layer, corresponding to a mixture of environmental and plume fluid. The segregated volume distribution Ω_{ij} is shown in figure 16(d), using a colouring with fluid that *has not* mixed with the environment ($\Omega < 0$) in blue and fluid that *has* mixed with the environment ($\Omega > 0$) in red to black. Figure 16(b) shows the unmodified volume distribution and figure 16(c) shows the cumulative flux volume distribution for illustrative purposes.

As shown in figure 15, a simple constraint on the largest accessible environmental buoyancy is the buoyancy at $z_{\max}$ in the initial local stratification. In fact, the local buoyancy gradient is modified as the plume pushes environmental fluid upwards, so $b|_{z_{\max}}$ is typically an overestimate for the largest buoyancy accessed via mixing. This constraint is shown as a vertical dashed line in figure 16(b)–(d), evidently an overestimate for this simulation. The largest buoyancy and tracer concentration at the bottom of the stratified layer is also a maximal constraint for the source line. This constraint is not indicated in figure 16 as the maximum buoyancy and tracer concentration arriving in the plume varies considerably in time.

To verify these ideas, it is useful to identify which regions of physical space correspond to the classes of fluid distinguished by the segregated volume distribution. Figure 16(a) shows a cross-section of the stratified layer in which regions with non-zero tracer concentration are coloured according to the segregated volume distribution; that is, each point in the physical domain has

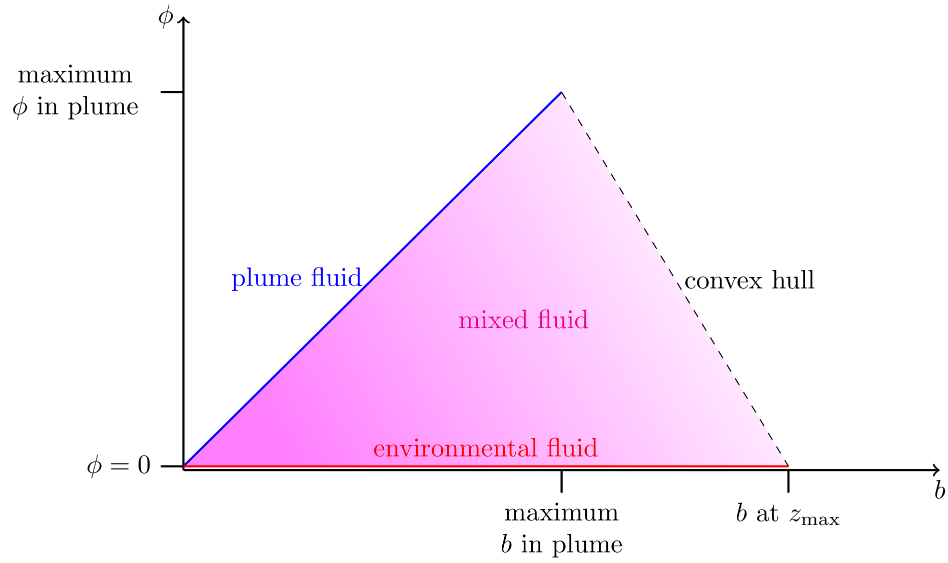

Figure 15: Schematic diagram of the segregated volume distribution and its physical interpretation.

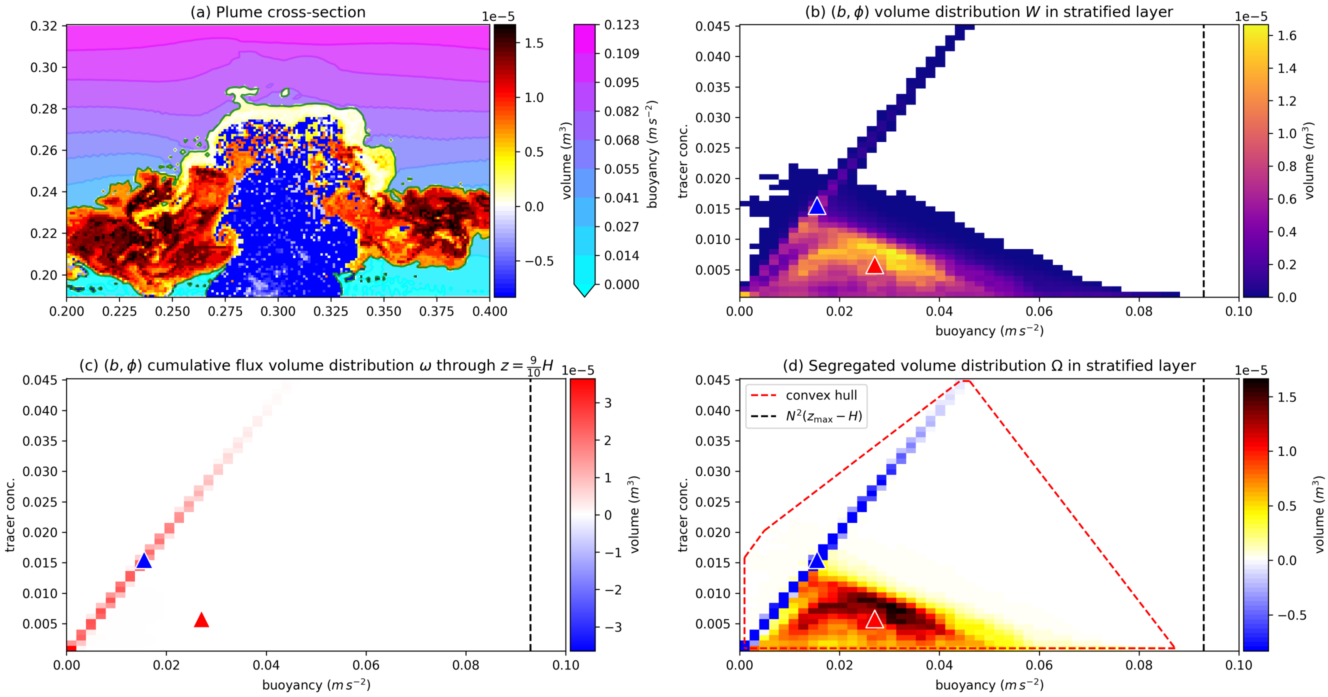

Figure 16: Composite figure of the construction of the segregated volume distribution with (b) the original volume distribution, (c) the cumulative flux volume distribution and (d) the segregated volume distribution. Panel (a) shows the plume cross-section with the plume fluid coloured according to the corresponding (b, ϕ) bin in panel (d). Data from the same simulation as figure 14, at $t = 15\,s$. The dashed black vertical line in (b)–(d) indicates the initial environmental buoyancy at $z_{\max}$. The red and blue triangles indicate the centre-of-mass of the unmixed plume fluid and the environmentally mixed fluid, respectively.

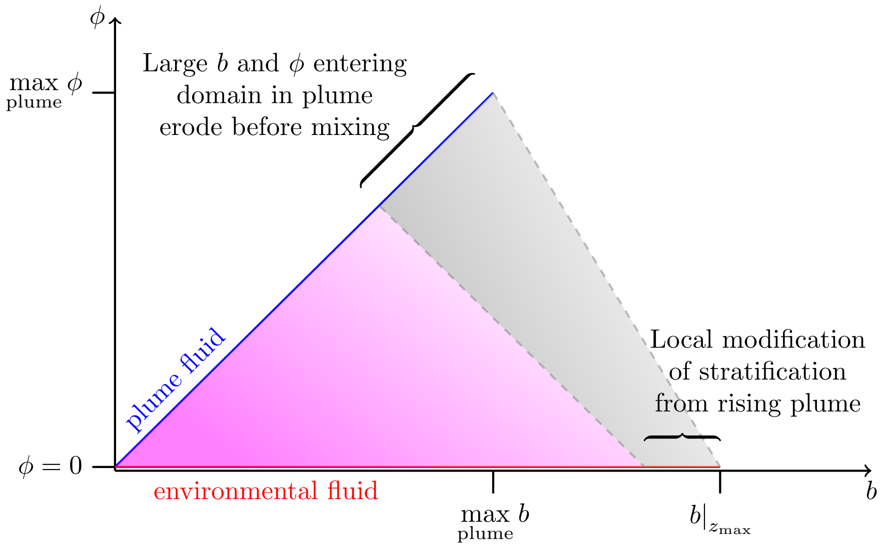

Figure 17: Schematic diagram of the accessible regions of the buoyancy-tracer volume distribution.

the colour of the bin in figure 16(d) containing the buoyancy and tracer concentration of that point. Where the tracer concentration vanishes, the environmental buoyancy is shown. The cross-section supports the interpretation of the segregated volume distribution as distinguishing plume fluid and environmentally mixed fluid; the blue, negative Ω regions highlight the rising component of the plume. At heights approaching $z_{\max}$, as the plume begins to overturn and mix with the surrounding environment, the colour suggests small Ω for fluid at these buoyancies and tracer concentrations, indicative of fluid in the process of moving from one class of fluid to the other via mixing. In the falling components of the plume either side of the plume cap, the colour gradually moves to red and black indicating positive Ω as further mixing homogenises the fluid toward the buoyancy and tracer concentration found in the large volume of fluid in the spreading intrusion at z_n.

This cross-section view of the corresponding segregated volume distribution is useful for supporting the physical interpretation of the results, but also for identifying regions of active mixing between plume fluid and the environment. Evidently most mixing occurs around the overturning plume cap, but there is also evidence of mixing on the fringes of the central rising column inside the plume. Moreover, we see that the mixing is not complete after fluid overturns near $z_{\max}$; further environmental fluid is entrained as fluid falls downwards and joins the intrusion at z_n.

4.3.3 Concentrated mixed region

It is evident in figure 16(d) that the mixed fluid does not occupy the entire convex hull shown in figure 15, for two reasons. Firstly, the largest values of buoyancy and tracer concentration in the plume are found in the largest eddies as they first enter the stratified layer. These eddies must collapse into smaller eddies before viscous diffusion can take place, which occurs via stirring as the eddies rise through the plume. However, as these eddies decay the buoyancy and tracer concentration homogenises with the surrounding plume fluid. Mixing between fluid parcels with these large values of buoyancy & tracer concentration and environmental fluid is therefore relatively uncommon. Moreover, as mentioned earlier, the environmental buoyancy of the initial stratification at $z_{\max}$ is an overestimate for the largest accessible environmental buoyancy due to modification of the local stratification as the rising plume pushes environmental fluid upwards. Significant accumulation of mixed fluid is therefore excluded from reaching certain parts of the convex hull, as indicated by the grey area in figure 17.

The centre-of-mass (CoM) is a useful indicator of the distribution of each class of fluid. The CoM of the pre-mixed (i.e. unmixed with environment) plume fluid is shown as a blue triangle whilst

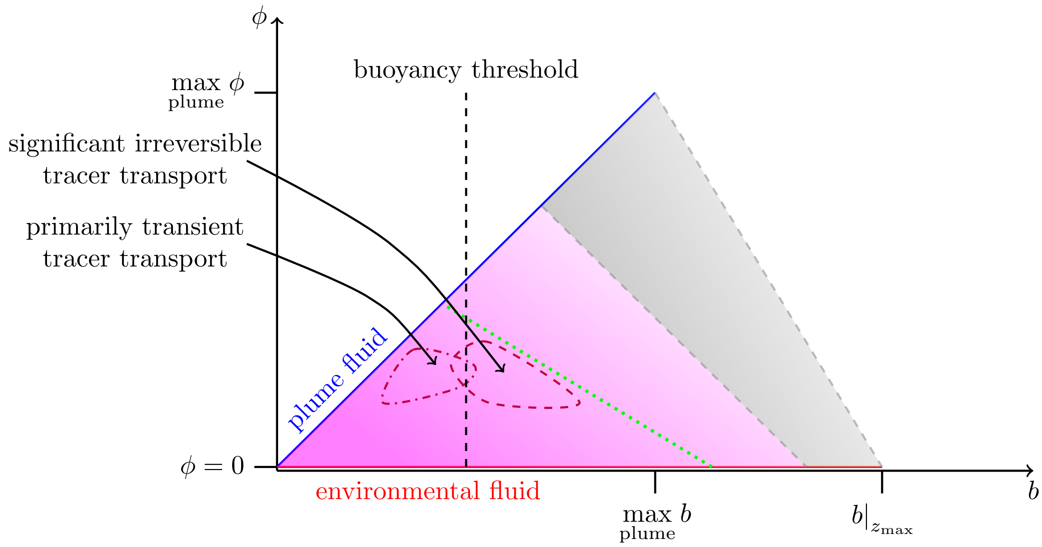

Figure 18: Schematic diagram of the buoyancy-tracer volume distribution and its relevance to the stratospheric hydration problem.

the CoM of the environmentally mixed plume fluid is shown as a red triangle in figure 16. The pre-mixed CoM is at much smaller buoyancy and tracer concentration than the largest values found as the plume enters the stratified region, supporting the above argument that most plume fluid – in particular, plume fluid with large tracer concentrations – mixes internally before mixing with the environment. The post-mixed CoM also supports the idea that the mixed fluid is generally confined to a small region of the available convex hull.

Figure 16(d) and the post-mixed CoM suggest that within the region of buoyancy-tracer space accessible to mixed fluid, the bulk of the volume lies in a much further constrained region with a concentrated peak in volume at intermediate buoyancy and tracer concentration. Figure 18 shows a schematic of this, with the region occupied by mixed fluid indicated by a dotted green line and the concentrated bulk of the fluid indicated by a purple dot-dashed & dashed line. It is exploration of this concentrated region that ultimately links back to the motivating atmospheric question. Simplistically, one might imagine that after the transient dynamics of a convective overshoot have settled, the distinction between tracer which remains in the stratosphere and tracer which settles back into the troposphere is some buoyancy threshold, indicated as a black dashed line in figure 18. If the mixed fluid is concentrated at buoyancies greater than this threshold, there is a large irreversible transport of tracer into the stratosphere. If the mixed fluid is concentrated at lower buoyancies than the threshold, there is only a small irreversible transport even if large tracer concentrations are transiently present in the stratosphere. Whilst this is a simplistic representation of the physical processes determining whether tracer remains in the stratosphere, particularly in the case of water vapour where distinct phases and temperature-dependent saturation of air play a crucial role, it is clear that we are interested in what sets the distribution of the mixed fluid within the accessible regions of the segregated volume distribution. Moreover, it is useful to understand what sets the boundaries of this concentrated region, and how the location of the concentrated region might depend on and be predicted by bulk properties of the penetrating plume.

5 Turbulent mixing

In the preceding section, we focused on methods of analysing the transport of passive tracer as a plume penetrates a stably stratified layer. In particular, we developed a method of identifying mixed plume and environmental fluid in a buoyancy-tracer volume distribution. In this section, we examine the characteristics of the mixing itself using a number of well established metrics of mixing activity and energy transfer. We will establish which metrics are the most useful for

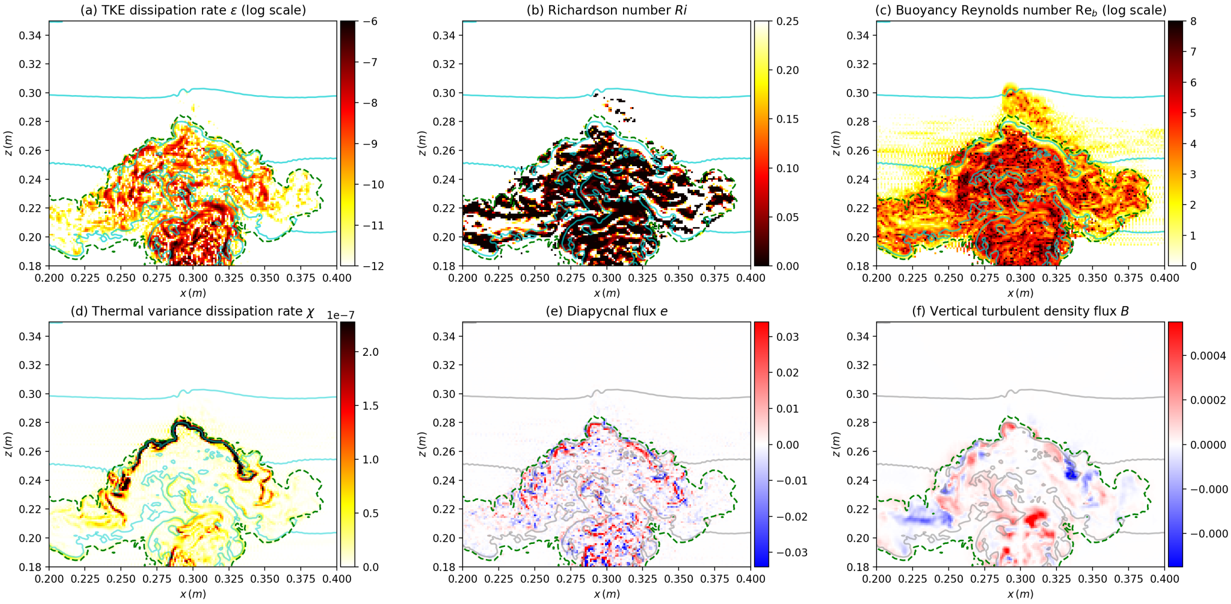

Figure 19: Cross-sections through the plume centreline of the penetration region, showing a snapshot of mixing metrics at time $t = 12\,s$ in a simulation with the same parameters as in figure 14. Green lines indicate the tracer surface $\phi = 10^{-3}$ and buoyancy contours are shown in grey or blue depending on the colourbar used for the metric.

understanding the mixing processes involved in convective penetration, and use the segregated volume distribution to establish some properties of the environmentally mixed plume fluid.

5.1 Mixing metrics

In the literature, many different metrics are used to characterise where mixing is strongest and which mechanisms are responsible for the mixing. Figure 19 shows a selection of these metrics, some of which are also useful for analysing the energetics of the problem, for an instantaneous snapshot of the plume in the stratified region. The time variation of these metrics is also of interest, but difficult to present clearly. The snapshot displayed here is chosen to be representative. The data presented in this section is from a simulation with $H = 20\,\mathrm{cm}$, $r_0 = 0.2\,\mathrm{cm}$, $F_0 = 0.15 r_0^2\,\mathrm{m}^4\mathrm{s}^{-3}$ and $N = 1.0\,s^{-1}$.

(a) The **Turbulent Kinetic Energy (TKE) dissipation rate** ε represents the conversion of kinetic energy into internal energy as a result of turbulent velocity gradients working against turbulent deviatoric stresses, defined as

$$\varepsilon \equiv 2\nu_{\text{eff}} \overline{\frac{\partial u_i'}{\partial x_j} \frac{\partial u_i'}{\partial x_j}} \tag{27}$$

where $\bar{\cdot}$ represents an appropriate average to isolate the turbulent velocity component $\boldsymbol{u'} = \boldsymbol{u} - \overline{\boldsymbol{u}}$. Note that strictly this is the *pseudo-dissipation*, a modified version of the dissipation which tends to simplify the form of equations relating to TKE, with a factor $\nu\overline{\partial_j u_i' \partial_i u_j'}$ subtracted that is small and introduces an error typically around 2%. The TKE dissipation rate represents a sink in the TKE evolution equation, and is positive definite. Physically, this represents the fact that the conversion of KE to internal energy is irreversible. Note that the spatially varying effective viscosity $\nu_{\text{eff}} = \nu + \nu_T$ is used so that sub-grid-scale contributions are accounted for. Large values of ε imply strong turbulent motion. In figure 19(a), ε is shown on a log scale due to the large variation. It is clear that ε is concentrated within the plume, as expected since strong turbulence is confined to the plume. Otherwise, there is little spatial structure to ε within the plume, although there are slightly larger amplitude variations in the centre of the plume and the overturning plume cap compared with the spreading intrusion.

(b) The **Richardson number** Ri is a dimensionless number representing the balance between buoyant and shear forces. It is defined differently depending on the context, for example Γ defined earlier. Here we consider the *local gradient* Richardson number, defined as

$$\mathrm{Ri} \equiv \frac{2\frac{\partial b}{\partial z}}{\left(\frac{\partial u}{\partial z}\right)^2 + \left(\frac{\partial v}{\partial z}\right)^2} \tag{28}$$

When $\mathrm{Ri} > \frac{1}{4}$, buoyancy tends to suppress shear-driven turbulence and the associated diapycnal transport is restricted towards molecular diffusion only, though other sources of turbulence may still provide diapycnal transport. When $\mathrm{Ri} < \frac{1}{4}$, buoyancy cannot suppress shear-driven turbulence and shear instabilities can develop, leading to mixing (Ivey et al., 2008). In figure 19(b), dark colours indicate susceptibility to shear instability, which is confined to the plume as expected since the surrounding region is stably stratified and quiescent. There is a distinct layering of the unstable regions, the lengthscale of which may be related to the volume-averaged vertical Taylor scale

$$l_z^2 = \frac{\langle u^2 + v^2 \rangle}{\langle \left(\frac{\partial u}{\partial z}\right)^2 + \left(\frac{\partial v}{\partial z}\right)^2 \rangle} \tag{29}$$

where $\langle \cdot \rangle$ denotes a volume average (Riley and deBruynKops, 2003). This scale may be related to the *volume-averaged* Richardson number Ri_V, defined as in (28) but with N^2 replacing $\partial_z b$, via a vertical Froude number

$$\mathrm{Fr}_l = \frac{2\pi u'_H}{N l_z} = \frac{2\pi}{\sqrt{2\mathrm{Ri}_V}} \tag{30}$$

where $u'_H = \langle u^2 \rangle^{1/2} = \langle v^2 \rangle^{1/2}$ is the horizontal root mean square velocity. There is also an unstable region slightly above the tracer and buoyancy contours which are closely aligned, indicating possible mixing and diapycnal transport of tracer as a result. These aspects require further investigation.

(c) The **buoyancy Reynolds number** Re_b is another dimensionless quantity used to characterise turbulent mixing in stratified flows, defined as

$$\mathrm{Re}_b \equiv \frac{\varepsilon}{\nu \frac{\partial b}{\partial z}} \tag{31}$$

Re_b is generally used in oceanographic contexts in combination with the Froude number, and it is generally suggested that active turbulence is only present when $\mathrm{Re}_b > 20$ (García-Villalba and del Álamo, 2011), though this does not necessarily hold in an atmospheric context – what determines energetic motion should be considered relative. As for ε, a log scale is used due to the wide range of values. In figure 19(c) the most energetic motions are, as expected, confined to the plume. In most of the plume, there is no clear spatial structure, though there are several relatively less energetic layers which coincide with relatively stable layers in the Ri plot. This suggests there is a strong buoyancy gradient in these layers, suppressing turbulence. Note the large amplitudes in the rising part of the plume indicating energy-containing large eddies. There are also relatively energetic motions outside of the tracer contours at the top of the plume cap, indicating possible turbulence which acts to mix the plume fluid with the surroundings.

(d) The **buoyancy variance dissipation rate** χ represents irreversible mixing via diffusion, defined as

$$\chi \equiv \kappa_{\text{eff}} \overline{|\nabla b'|^2} \tag{32}$$

where $\kappa_{\text{eff}} = \kappa_b + \kappa_{b,T}$ is the effective diffusivity of buoyancy, accounting for sub-grid-scale contributions as with the effective viscosity. Large values of χ imply strong diffusive mixing and a smoothing of the buoyancy gradient as a result. In figure 19(d) we find the strongest diffusive mixing occurring at the top of the plume, as expected since this region has the strongest buoyancy gradients. Other regions of strong mixing are in the subsiding regions near the plume top, as more buoyant environmental fluid is pulled down introducing strong buoyancy gradients.

(e) **Vertical turbulent buoyancy flux** B measures the net upwards transport of buoyancy by turbulence, representing the conversion of kinetic energy (KE) into potential energy (PE) when $B > 0$ as relatively heavy fluid is moved upwards, and vice versa when $B < 0$. Here, we define

$$B = \overline{b'w'} \tag{33}$$

where b' and w' are the turbulent components, calculated as the anomaly from the azimuthally averaged buoyancy and vertical velocity. In future work, this could be modified to account for both spatial and temporal covariance as in appendix A. In figure 19(e) we generally find $B > 0$ in the rising component of the plume and $B < 0$ in falling components of the plume. Physically this indicates that turbulence in the plume gradually converts KE into PE as the plume rise slows. Once the plume fluid overturns, the stored PE is then converted back to KE. Relatively little energy conversion is seen in the spreading intrusion. At the top edges of the plume, there is some conversion of KE to PE, further indicating mixing.

(f) The **diapycnal flux** is the normal flux across an isopycnal surface, sometimes referred to as the diapycnal entrainment velocity e. We have

$$e = w - \frac{\partial z}{\partial \tilde{t}} - u\frac{\partial z}{\partial \tilde{x}} - v\frac{\partial z}{\partial \tilde{y}} \tag{34}$$

where $\tilde{}$ indicates the calculation of partial derivatives with ρ (or equivalently b) fixed, i.e. on isopycnal surfaces (De Szoeke and Bennett, 1993). It may be shown that

$$e = \frac{\partial z}{\partial b}\frac{\mathrm{D}b}{\mathrm{D}t} = \kappa_{\text{eff}}\frac{\partial z}{\partial b}\nabla^2 b \tag{35}$$

where, for the purposes of reducing noise, we use $\frac{\partial z}{\partial b} \approx N^{-2}$ as a global average. Positive values of e represent the transport of fluid to greater buoyancy and the opposite for $e < 0$. In figure 19(f) regions of large diapycnal transport are confined to the plume, as expected. There are large amplitude variations in the bottom centre of the plume as large eddies travel upwards and entrain fluid. Large positive values are found at the top, overturning part of the plume, further supporting the implication of diapycnal transport found in plots of Ri, ε and χ. Similarly, in the subsiding component of the plume there is negative e as a result of more buoyant environmental fluid mixing with less buoyant plume fluid.

In the literature, some of these definitions use the squared buoyancy frequency $N^2 = \frac{\partial b}{\partial z}\big|_{t=0}$ as a measure of the buoyancy gradient. However, in the region of interest, the buoyancy gradient is heavily modified by the impinging plume, in which case the dynamical gradient $\partial_z b$ is a more useful measure of the local buoyancy gradients. In figure 19, the local buoyancy gradient is used in Ri as turbulent shear instabilities depend on the strength of the *local* shear. Similar, the local buoyancy gradient is used in Re_b to indicate energetic turbulent motions acting to strengthen the *local* buoyancy gradient.

5.2 Properties of pre- and post-mixed fluid

To characterise the mixing properties of regions of the plume distinguished by the segregated volume method, we investigate the values of selected mixing metrics in each region. This allows us to understand how the turbulence changes as fluid arrives, mixes, and settles into the intrusion. In this way, we verify the ideas established thus far on the physical interpretation of the pre- and post-mixed fluid highlighted in the segregated volume distribution, and work towards understanding the mixing mechanisms involved in convective penetration.

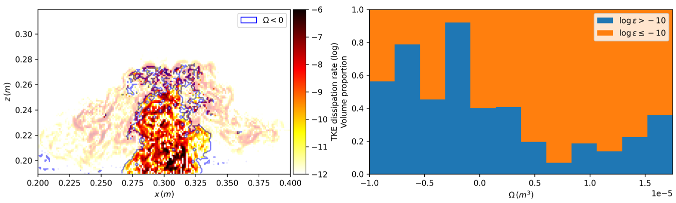

(a) Turbulent kinetic energy dissipation rate ε. Log scale used in right panel. Threshold $\log \varepsilon > -10$.

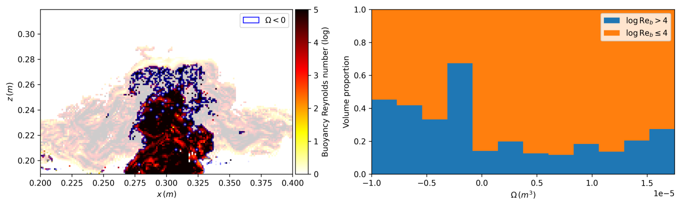

(b) Buoyancy Reynolds number Re_b. Log scale used in right panel. Threshold $\log \mathrm{Re}_b > 4$.

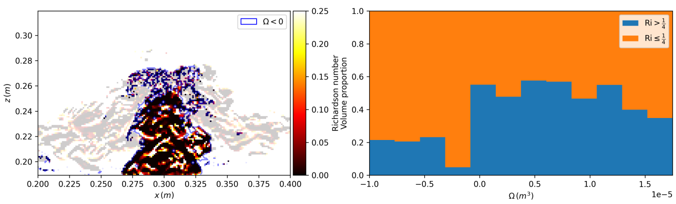

(c) Richardson number Ri. Threshold $\mathrm{Ri} > \frac{1}{4}$.

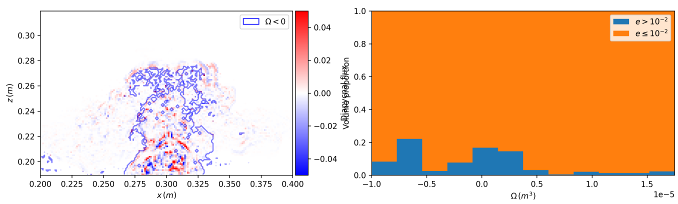

(d) Diapycnal flux e. Threshold $e > 10^{-2}$.

Figure 20: Volume proportion plots of a selection of mixing metrics discussed in section 5.1 (left). Plume cross-sections showing the relevant metric and unmixed plume regions with $\Omega < 0$ highlighted (right). Data from the same simulation as figure 14, at $t = 15\,s$.

In this section we will examine the mixing characteristics as follows. The range of volume Ω represented in the segregated volume distribution (see figure 16) is separated into equal sized bins. Given a range of volume, we identify the fluid in the stratified layer with buoyancy and tracer concentration corresponding to values of Ω lying in that range. We then compute the proportion of this fluid where some metric exceeds a threshold set based on figure 19. Repeating for all bins, we form a 2D plot with segregated volume distribution weight Ω on the horizontal axis and the proportion on the vertical axis. The threshold is chosen to identify particular properties: for example, when considering the diapycnal flux e we choose a threshold 10^{-2} so that we can determine which values of Ω correspond to fluid where large amounts of tracer are being transported to greater buoyancies. Alongside the volume proportion plot we also show a cross-section of values of the relevant metric. Regions of the plume with corresponding segregated volume distribution weight $\Omega < 0$ are highlighted to distinguish parts of the plume not yet mixed with the environment, to aid interpretation of the results. We use data from the same simulation as figure 19, with $H = 20\,\mathrm{cm}, r_0 = 0.2\,\mathrm{cm}, F_0 = 0.15 r_0^2\,\mathrm{m}^4\mathrm{s}^{-3}$ and $N = 1.0 s^{-1}$. The volume proportion plots are evaluated at $t = 15\,s$.

(a) Figure 20(a) shows the volume proportion plot for the TKE dissipation rate ε using a log-scale and a threshold $\log \varepsilon > -10$, indicating strong turbulent motion. We find that large proportions of pre-mixed plume fluid exhibit turbulent motion, as expected in the rising plume. Moreover, there is also a large proportion of turbulent fluid in regions with $\Omega \approx 0$, interpreted as regions where active mixing is occurring. The plume cross-section demonstrates that the values of ε found within the environmentally mixed fluid are smaller, in particular within the spreading intrusion. In the subsiding fluid around the plume cap, where $\Omega \approx 0$ but Ω is increasing, strong turbulent motion is still present.

(b) The buoyancy Reynolds number Re_b indicates turbulent and energetic motion where it is large. The choice of threshold is based on figure 19, since what constitutes an energetic motion is relative and depends on the system. We choose $\log \mathrm{Re}_b > 5$ as the threshold. The volume proportion plot in figure 20(b) indicates that the most energetic motions lie within the rising plume, with a lower proportion of energetic motions in fluid with $\Omega \gtrapprox 0$. The plume cross-section suggests that in the spreading intrusion, Re_b reaches similar maxima to within the rising plume, but there are also more regions within the intrusion with smaller Re_b.

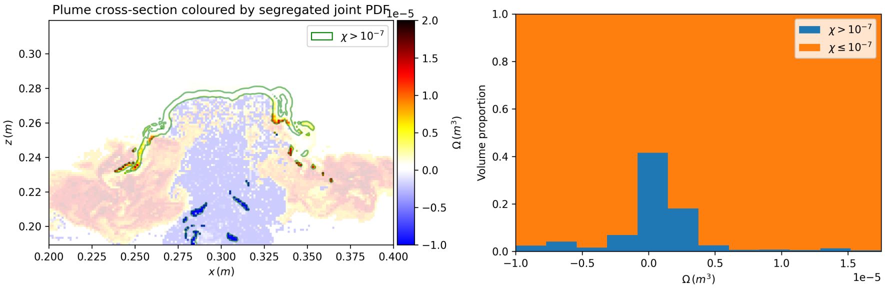

Figure 21: Volume proportion plot for buoyancy variance dissipation rate χ with threshold $\chi > 10^{-7}$ (left). Plume cross-section coloured according to segregated volume distribution with large χ region highlighted (right). Data from the same simulation as figure 14, at $t = 15\,s$.

(c) The volume proportion plot for the Richardson number Ri is shown in figure 20(c). The natural choice of threshold is $\mathrm{Ri} > \frac{1}{4}$, which indicates regions in which buoyancy tends to inhibit shear instability. We find that unmixed plume fluid $\Omega < 0$ is dominated by regions with $\mathrm{Ri} \leq \frac{1}{4}$, suggesting a susceptibility for shear instability to arise. In regions with mixed environmental and plume fluid, the proportion is more even between regions with buoyancy dominating and regions with shear dominating. This observation is supported by the plume cross-section.

(d) Figure 20(d) shows the volume proportion plot for the diapycnal flux e. Here, we examine regions where tracer can be transported up-gradient across buoyancy surfaces by choosing the threshold $e > 10^{-2}$. There are two groups of Ω with non-trivial volume proportion of fluid with $e > 10^{-2}$. First, in support of our earlier conclusions on the physical interpretation of fluid with $\Omega \approx 0$, we find up-gradient transport of tracer, indicating active mixing between plume fluid containing tracer and more buoyant environmental fluid. Similarly we find active mixing in regions with $\Omega < 0$, as expected as the turbulent motions mix tracer in the rising plume.

Finally, we consider the volume proportion plot for the buoyancy variance dissipation rate χ. This is arguably the best indicator of active mixing, as it signifies intense buoyancy gradients which support strong diffusion. Combined with active turbulent motion which acts to stretch the buoyancy surfaces across which diffusion acts, significant transport of tracer across buoyancy surfaces is possible. As with the buoyancy Reynolds number, the choice of threshold is somewhat arbitrary and guided by figure 19; we choose $\chi > 10^{-7}$ to distinguish intense buoyancy gradients. Alongside the volume proportion plot in figure 21, we show a cross-section of the plume coloured according to the segregated volume distribution (as in figure 16(a)) with the regions with $\chi > 10^{-7}$ highlighted. We find that other than in the rising plume in which sharp buoyancy gradients occur within large eddies, the main region with intense buoyancy gradients is at the edge of the overturning plume cap and the subsiding regions surrounding it. In section 4.3.2 we identified this region as predominantly composed of fluid with $\Omega \approx 0$, indicating fluid in the process of mixing with the environment. This is supported by the volume proportion plot, with the greatest proportions of fluid with $\chi > 10^{-7}$ found where $\Omega \approx 0$.

Together, these results help to characterise the fluid in distinct regions of the plume. Broadly, we can consider three regions: the rising plume, which has not mixed with the environment; the overturning and subsiding plume cap, which contains fluid actively mixing with the environment; and the spreading intrusion. In the rising plume, the results discussed here imply there is strong turbulent and energetic motion which dominates buoyancy and allows shear instabilities to break down and homogenise large eddies, resulting in strong diapycnal fluxes. There are regions of strong buoyancy gradients, but these quickly decay as the plume rises and mixes internally. As the rising plume reaches $z_{\max}$, mixing between the plume and the environment occurs as the fluid overturns and begins to subside. In this region we find strong buoyancy gradients with strong turbulence persisting in the rising fluid. Compared to the rising component, motions are less energetic as large amounts of kinetic energy have been converted to potential energy which is then released as fluid subsides. Whilst the shear is weaker in this region and shear instabilities are better suppressed than in the rising plume, the strong buoyancy gradients result in strong diapycnal fluxes. Finally, in the spreading intrusion near z_n, we find less energetic motion and weaker turbulence, with weaker diapycnal fluxes as a result.

6 Future work

Before concluding the research presented in this essay, we discuss possible routes for future study. The analysis developed so far has been applied to simulations with a single set of parameters, to gain an understanding of the phenomenology of the problem, the mixing characteristics present, and the tracer transport taking place. The natural progression is then to compare these results when one parameter is varied; the changes indicate which aspects of the problem are dependent on which parameters. The understanding gained may offer a route to deriving scalings for the size and location of the concentrated region of tracer in the segregated volume distribution. In the context of the motivating atmospheric problem, there are many other aspects of convective penetration which may aid in understanding hydration of the lower stratosphere. Here, we discuss two topics which formalise ideas already discussed.

6.1 Diapycnal flux

The diapycnal flux is a key property to understand, as ultimately to answer the question of 'how much tracer makes it to a given height?' it is valuable to instead answer 'how much tracer makes it to a given isopycnal surface?', in which case, the cumulative diapycnal flux goes some way to answering that question. Furthermore, in the atmospheric context, the diapycnal flux holds even more prominence since the key process for retaining water vapour in the stratosphere is thought to be the formation of a vapour-rich pocket of air above deep convection which may then be entrained via the distortion of isentropic (constant potential temperature) surfaces by shear-induced turbulence (Dauhut et al., 2018). It is therefore essential to understand how much tracer can reach each isentropic surface – or isentrope – indicating whether a vapour-rich pocket may form.

The diapycnal flux e discussed in section 5.1 is a *local* and *instantaneous* measure of the velocity across buoyancy surfaces. Therefore, whilst indicating intense regions of diapycnal tracer transport, it does not provide information on the buoyancy surfaces across which the transport takes place, nor quantify the amount of tracer that is transported. We may have strong tracer transport across buoyancy surfaces which correspond to isentropes lying in the troposphere but are transiently distorted into the lower stratosphere by a rising convective overshoot. In that case, the tracer transport is not significant as the restratification process will bring the tracer back into the troposphere. It is therefore useful to use the z^* formalism, which implicitly accounts for the restratification process by construction. We can then examine the diapycnal flux of a tracer ϕ across buoyancy surfaces with z^* lying in the stratosphere.

The z^* formalism uses a sorted density (or buoyancy) coordinate z_* following Winters and D'Asaro (1996), defined for a given value of density ρ_* by

$$z_*(\rho_*, t) = \frac{1}{A_d} \int_{\rho(\boldsymbol{x},t) \geq \rho_*} \mathrm{d}V \tag{36}$$

where A_d is the horizontal area of the domain V. Note that this may be reformulated with any scalar ϕ in place of the scalar density field ρ. When using density (or equivalently buoyancy), z_* may be interpreted as the vertical coordinate after the restratification process is complete. Given the constant source of buoyancy in this problem, restratification must be interpreted as happening after the plume (representing a convective overshoot) has been subsided and is no longer penetrating the stratified layer. Nonetheless, this formalism can be used to form an evolution equation for the mean value $\langle \phi \rangle_{z_*}$ of tracer ϕ on a z_* surface, which is defined by Penney et al.

(2020) as

$$\langle\phi(z_*,t)\rangle_{z_*} = \frac{1}{A_d}\frac{\partial}{\partial z_*}\int_{\rho(\boldsymbol{x},t)\geq\rho_*}\phi(\boldsymbol{x},t)\mathrm{d}V \tag{37}$$

and evolves according to

$$\frac{\partial}{\partial t}\langle\phi\rangle_{z_*} = \frac{\partial}{\partial z_*}\left(\frac{\kappa_\phi}{\kappa_\rho}K_\rho\frac{\partial\langle\phi\rangle_{z_*}}{\partial z_*}\right) + \frac{\partial}{\partial z_*}\left(\frac{\partial z_*}{\partial\rho_*}\langle(\kappa_\phi\nabla\phi'\cdot\nabla\rho - \kappa_\rho\phi'\nabla^2\rho)\rangle_{z_*}\right) \tag{38}$$

where K_ρ is the effective diffusivity for density. The concept of effective (or eddy) diffusivity is useful as a parameterisation of mixing. Penney et al. (2020) investigate the importance of the final 'eddy' term of (38), the idea being that if its cumulative effects are small then it can be ignored and we can use K_ρ as an eddy diffusivity for ϕ when modified by the factor κ_ϕ/κ_ρ.

In a related manner, Winters and D'Asaro (1996) define a general turbulent eddy diffusivity K_ϕ for tracer ϕ as

$$K_\phi \equiv -\phi_d\frac{\mathrm{d}z_*}{\mathrm{d}\phi} \tag{39}$$

where ϕ_d is the diascalar flux

$$\phi_d = -\kappa_\phi\frac{\mathrm{d}z_*}{\mathrm{d}\phi}\langle|\nabla\phi|^2\rangle_{z_*} \tag{40}$$

The quantity ϕ_d and the mean tracer $\langle\phi\rangle_{z^*}$ are powerful tools for understanding diapycnal tracer transport which may be incorporated into the analysis presented in sections 4 and 5.

6.2 Mixing efficiency

In most physical systems, energy is a useful tool for understanding the dynamics. In this essay we have discussed some aspects of energetics, for example turbulent kinetic energy and the vertical turbulent buoyancy flux which represents conversion of KE to PE. In flows with a stable stratification, a component known as the 'background potential energy' of the potential energy is not available for conversion to kinetic energy. The remaining portion, the 'available potential energy', is available to do work and may be irreversibly converted to background potential energy via mixing. The conversion between various forms of energy is detailed in Winters et al. (1995) using an 'energy diagram' with conversion terms between background potential, available potential, kinetic, external, and internal energy. The energy budget of restratification is accounted for using the z^* formalism. A crucial aspect of understanding geophysical flows involving mixing is to quantify the available potential energy available for mixing, .

A concept often used to describe the energetics of mixing is the mixing efficiency $\mathcal{E}$, which seeks to relate the energy expended in turbulent mixing with the actual mixing achieved (Davies Wykes et al., 2015). It can be defined in different ways depending on the context (Gregg et al., 2018). A useful definition which incorporates the z_* formalism discussed here is

$$\mathcal{E} = \frac{\text{Change in background potential energy due to mixing}}{\text{Total energy expended}} \tag{41}$$

The background potential energy E_b may be defined as the minimum potential energy attainable through an adiabatic redistribution of ρ. Using the concept of z_* defined above as a vertical position in a redistributed density field $\rho(z_*)$, we may write E_b as

$$E_b = g\int_V \rho z_*(\boldsymbol{x},t)\,\mathrm{d}V \tag{42}$$

The total potential energy E_p is a combination of the background potential energy E_b and the available potential energy E_a, the accessible potential energy which could be released in an adiabatic redistribution from $\rho(\boldsymbol{x},t)$ to $\rho(z_*)$. We have

$$E_a = g\int_V \rho\left(z - z_*(\boldsymbol{x},t)\right)\,\mathrm{d}V \tag{43}$$

such that the total potential energy $E_p = E_b + E_a$.

Winters et al. (1995) derive evolution equations for these quantities so that changes in PE due to diabatic mixing and adiabatic processes may be separated. The change in E_b may be expressed as

$$\frac{\mathrm{d}E_b}{\mathrm{d}t} = -g \oint_S \psi \boldsymbol{u} \cdot \mathrm{d}\boldsymbol{S} + \kappa_\rho g \oint_S z_* \nabla\rho \cdot \mathrm{d}\boldsymbol{S} + \kappa_\rho g \int_V -\frac{\mathrm{d}z_*}{\mathrm{d}\rho} |\nabla\rho|^2 \,\mathrm{d}V \tag{44}$$

where $\psi = \int^\rho z_*(\hat{\rho})\,\mathrm{d}\hat{\rho}$. The first and second terms account for advection and diffusion across the surface S bounding V. The third term is of central importance, accounting for material changes in ρ due to diapycnal mixing, which acts to increase background potential energy E_b. To apply this formulation to convective penetration, an appropriate choice of V must be made. Since the entrainment in the rising plume is not the focus, a natural choice for V is the stratified region $z \geq H$. This also conveniently does away with the need for a buoyancy source in the governing equations and instead an input flux on the bottom boundary accounts for the buoyancy input of the plume. The governing equation (44) for E_b would need modification to include this additional flux.

In the context of the atmospheric problem, the advantage of using mixing efficiency is a simplistic way to determine how much hydration we expect from a certain input of energy from a convective overshoot. The mixing efficiency yields an estimate for the mixing achieved from a given energy input and by further understanding the irreversible tracer transport that arises from some intensity of mixing characteristic of convective penetration in the lower stratosphere, we may form a rough (but convenient) estimate for the water vapour transport. Moreover, an investigation of the energetics of the convective penetration problem as a whole aid in understanding how large-scale atmospheric models might estimate the energy involved in convective overshoots relative to wider thunderstorm complexes.

7 Conclusion

In this essay, we begun with the problem of quantifying irreversible water vapour transport in the tropical tropopause layer via convective overshoots from large thunderstorm complexes. To tackle this, we reduced the complex atmospheric problem to the idealised fluid dynamical representation of a turbulent plume penetrating a stably stratified layer. Having verified the capability of numerical simulations to represent the essential physics of a buoyant plume, we demonstrated that simulations of convective penetration reliably represent laboratory experiments of the same setup. We then focused on two aspects of convective penetration: developing methods of analysing the tracer transport taking place and characterising the turbulent mixing producing this transport. We first introduced a tracer PDF in buoyancy coordinates, before moving to buoyancy-tracer space and considering the volume distribution in the stratified layer, in which mixing manifests as relocation of volume within the distribution, representing the homogenisation of the buoyancy and tracer concentration of the corresponding fluid parcels. We introduced a segregated volume distribution which accounts for the continuous input of buoyancy and tracer by the plume, and discussed its interpretation as distinguishing fluid arriving in the plume from that which has mixed with the surrounding stratified environment. Moreover, we identified the regions of most intense mixing between the plume and environment, which surround the plume cap and extend downwards with the subsiding fluid. We then discussed metrics which quantify the intensity of mixing, its driving mechanisms and the diapycnal tracer transport that results. Using the segregated volume distribution, we characterised the properties of the rising plume, as well as the regions of active mixing between the plume and environment, and the spreading intrusion of mixed fluid. We found that active turbulence in the rising plume erodes large tracer concentrations carried by large eddies entering the stratified layer, and that intense buoyancy gradients and energetic turbulent motion at the egde of the plume cap produce significant diapycnal transport, efficiently mixing plume fluid with the environment. Further characterising the mixed fluid that arises in the segregated volume distribution offers a way to quantify the irreversible transport of tracer by the plume and its dependence on key quantities, which provides a step towards understanding the stratospheric hydration problem.

Beyond comparing changes in our current analyses under varied stratification strength, there are a number of questions to be considered further. Complicating factors in the atmospheric case which were omitted in idealising the problem can be re-introduced to determine their influence. Some of these complexities relate to the atmospheric setup, and some to the physical properties of tracers, passive or otherwise. To better emulate the atmospheric environment, we could introduce a large-scale shear in the stratified layer which may promote shear-driven turbulence, or a weak stratification in the lower layer that is currently uniform. At present, the background buoyancy profile is simplified and neglects the complex nature of the UTLS in which the stratification gradually adjusts from tropospheric to larger stratospheric values; losing the distinction between a stratified and uniform layer will inevitably alter the penetration process and possibly the resulting tracer transport. In the atmosphere, one might consider a convective overshoot as originating from a central plume which forms the main component of a thunderstorm. The surrounding cloud environment is clearly not quiescent and crucially, water vapour is present. The importance of this observation could be tested by introducing an ambient source of tracer in the lower layer, which will be entrained into the plume and may increase tracer concentrations at the outer edges, but may also reduce the buoyancy of fluid parcels carrying tracer into the stratified layer. Whether the overall tracer transport is enhanced or not is an interesting question since we have found that it is the central regions of the plume which reach $z_{\max}$ that tend to mix with the environment most effectively. Finally, to bring us closer to the stratospheric hydration problem itself, simple representations of the thermodynamics of water vapour can be incorporated into the simulations. For example, the effects of sublimation and saturation can be modelled using multiple passive tracers which represent distinct phases of water.

A Post-processing method for numerical simulations

The DIABLO solver uses a 3D Cartesian coordinate system, with a horizontally uniform grid with cell widths $\Delta x = \Delta y$. High resolution simulations produce large amounts of data, so for practical reasons we reduce the data from 3D coordinates (x, y, z) to 2D axisymmetric cylindrical coordinates (r, z) by azimuthally averaging, with the plume centreline as the axis $r = 0$. To perform an azimuthal average, the 3D grid is discretised into cylindrical shells with axes aligned with the plume centreline, each with thickness $\Delta r \equiv \Delta x = \Delta y$. Denoting each shell as S_i with $i = 0, 1, \cdots, N_x/2 - 1$ we have

$$S_i \equiv \{(x, y) \mid i\Delta x \leq \sqrt{x^2 + y^2} \leq (i + 1)\Delta x\} \tag{45}$$

The azimuthal average of a variable χ at radius r and height z is then

$$a(\chi) = \frac{1}{N} \sum_{\text{shell}} \chi_i(r, z) \tag{46}$$

where $\{\chi_i(r, z)\}$ are the observations of χ from the cylindrical shell containing the radius r at height z and N is the total number of such observations.

The decomposition of the flow into mean and turbulent components requires an appropriate choice of mean. Under the assumption of statistical steadiness and statistical homogeneity in the azimuthal direction, the observed values of a variable χ at fixed (r, ϕ) are i.i.d. random variables, with expected value (mean) estimated by the combined azimuthal and time average. The (total) time average of a sequence of observations χ_i with time steps Δt_i over total time t_{run} is

$$t(\chi) = \frac{1}{t_{\text{run}}} \sum_i \chi_i \Delta t_i \tag{47}$$

where χ_i are observations at a 3D point (x, y, z) or 2D point (r, z) as desired. The mean component of a variable χ is then $\overline{\chi} = t(a(\chi)) = a(t(\chi))$ since the two averages commute. Note that t and a are idempotent. The turbulent component of a variable χ is composed of two terms; spatial fluctuation and temporal fluctuation. The spatial fluctuation $a'(\chi) = \chi - a(\chi)$ is the difference between χ and its azimuthal average at each point. The temporal fluctuation $t'(\chi) = a(\chi) - t(a(\chi))$

is the difference between the azimuthal average of χ and the total mean of χ. The Reynolds' decomposition of a variable χ is then

$$\chi = \overline{\chi} + \chi' \equiv t(a(\chi)) + a'(\chi) + t'(\chi) \tag{48}$$

The covariance of two variables χ and ψ is defined as

$$\overline{\chi'\psi'} \equiv \overline{\chi\psi} - \overline{\chi}\overline{\psi} \tag{49}$$

Using $\chi' = a'(\chi) + t'(\chi)$ and assuming spatial and temporal fluctuations are uncorrelated so that $\overline{a't'} \equiv 0$ for any variables, then

$$\overline{\chi'\psi'} = t(a(a'(\chi)a'(\psi))) + t(a(t'(\chi)t'(\psi))) \tag{50}$$

where the first term represents spatial covariance and the second term represents temporal covariance.

B Limitations of numerical simulations

The DIABLO LES of a buoyant plume exhibits a number of limitations. Some of these are limited to the specific unstratified configuration considered in the first section, in which there is no vertical limit on the plume evolution. For example, with the introduction of a stratified layer the plume does not reach the top boundary, so the associated pressure variation and overturning circulation limitations are not present. The presence of a buoyancy source but no sink in the domain remains a limitation when stratification is introduced, as the local ambient stratification will be modified by the buoyancy input. This places a limitation on the length of time that simulations can be run. Similarly, time limitations arise from the generation of internal gravity waves and their interference, as well as the radial spreading of any intrusions. One way to allow an intrusion to spread for longer is to increase the size of the domain. However, this limits the resolution that can be achieved whilst maintaining practical use of computer resources. Furthermore, reduced resolution means more small-scale turbulence must be captured by the LES model and as a result the turbulence characteristics, and therefore the mixing properties of the flow, may become more sensitive to the choice of model.

The vertical size of the domain, and the depth of the unstratified layer, is limited by the decay of source effects in the plume generation. As seen in figures 2, 4 and 5, the source effects only become negligible around $z/r_0 \gtrapprox 30$, so the unstratified plume generation region must be large enough to allow the plume to become fully developed before penetrating the stratified layer when introduced. Note that this is sensitive to the method of initiating turbulence, as other methods may reduce the lengthscale over which source effects decay and this must be tested in each simulation configuration. Finally, our volumetric forcing method limits the types of plume which can be simulated, as some inertial forcing is introduced resulting in $\Gamma < 1$. The forcing profile and the momentum equation coupling strength must be tested in each simulation configuration to achieve the desired pre-penetration plume dynamics. Nonetheless, the volumetric forcing method is advantageous compared to a simple buoyancy gradient at the bottom boundary. The effect of Gibbs ringing may be reduced by controlling the source radius, and 'pinching' of the plume where inflow dominates the diffusive boundary buoyancy flux is reduced; note the 'pinching' above the forcing region in figure 2 still present, but significantly improved from early test simulations with a simple buoyancy gradient on the boundary. Note that regardless of the simulation setup, the prescribed profiles of w and b are for an unstratified environment, since the forcing region is shallow enough that the effects of stratification are not felt.

References

J. K. Ansong and B. R. Sutherland. Internal gravity waves generated by convective plumes. *J. Fluid Mech.*, 648:405–434, 2010.

J. K. Ansong, P. J. Kyba, and B. R. Sutherland. Fountains impinging on a density interface. *J. Fluid Mech.*, 595:115–139, 2008.

M. P. Baldwin, L. J. Gray, T. J. Dunkerton,

K. Hamilton, P. H. Haynes, W. J. Randel, J. R. Holton, M. J. Alexander, I. Hirota, T. Horinouchi, D. B. A. Jones, J. S. Kinnersley, C. Marquardt, K. Sato, and M. Takahashi. The Quasi-Biennial Oscillation. *Revs. Geophys.*, 39:179–229, 2001.

L. J. Bloomfield and R. C. Kerr. Turbulent fountains in a stratified fluid. *J. Fluid Mech.*, 358: 335–356, 1998.

J. Craske. *Unsteady turbulent jets and plumes.* PhD thesis, Imperial College London, Department of Civil and Environmental Engineering, 2016.

J. Craske and M. van Reeuwijk. Energy dispersion in turbulent jets. Part 1. Direct simulation of steady and unsteady jets. *J. Fluid Mech.*, 763: 500–537, 2015.

T. Dauhut, J.-P. Chaboureau, J. Escobar, and P. Mascart. Large-eddy simulations of hector the convector making the stratosphere wetter. *Atmos. Sci. Lett.*, 16(2):135–140, 2015.

T. Dauhut, J-P. Chaboureau, P. H. Haynes, and T. P. Lane. The mechanisms leading to a stratospheric hydration by overshooting convection. *J. Atmos. Sci.*, 75(12):4383 – 4398, 2018.

M. S. Davies Wykes, G. O. Hughes, and S. B. Dalziel. On the meaning of mixing efficiency for buoyancy-driven mixing in stratified turbulent flows. *J. Fluid Mech.*, 781:261–275, 2015.

M. S. Davies Wykes and S. B. Dalziel. Efficient mixing in stratified flows: Experimental study of a rayleigh–taylor unstable interface within an otherwise stable stratification. *J. Fluid Mech.*, 756: 1027–57, 2014.

R. A. De Szoeke and A. F. Bennett. Microstructure fluxes across density surfaces. *J. Phys. Oceanography*, 23:2254–2264, 1993.

B. J. Devenish, G. G. Rooney, and D. J. Thomson. Large-eddy simulation of a buoyant plume in uniform and stably stratified environments. *J. Fluid Mech.*, 652:75–103, 2010.

M. R. Flynn and B. R. Sutherland. Intrusive gravity currents and internal gravity wave generation in stratified fluid. *J. Fluid Mech.*, 514:355–383, 2004.

U. Frisch. Turbulence: The Legacy of A.N. Kolmogorov. *Astrophys. Lett. and Comm.*, 1995.

S. Fueglistaler, A. E. Dessler, T. J. Dunkerton, I. Folkins, Q. Fu, and P. W. Mote. Tropical tropopause layer. *Rev. Geophys.*, 47(1), 2009.

M. García-Villalba and J. C. del Álamo. Turbulence modification by stable stratification in channel flow. *Physics of Fluids*, 23(4):045104, 2011.

M.C. Gregg, E.A. D'Asaro, J.J. Riley, and E. Kunze. Mixing Efficiency in the Ocean. *Annu. Rev. Mar. Sci.*, 10:443–473, 2018.

G.R. Hunt and H.C. Burridge. Fountains in Industry and Nature. *Annu. Rev. Fluid Mech.*, 47(1): 195–220, 2015.

G.N. Ivey, K.B. Winters, and J.R. Koseff. Density Stratification, Turbulence, but How Much Mixing? *Annu. Rev. Fluid Mech.*, 40(1):169–184, 2008.

E. J. Jensen, A. S. Ackerman, and J. A. Smith. Can overshooting convection dehydrate the tropical tropopause layer? *J. Geophys. Res. Atmos.*, 112(D11), 2007.

T. P. Lane and M. J. Reeder. Convectively Generated Gravity Waves and Their Effect on the Cloud Environment. *J. Atmos. Sci.*, 58(16):2427–2440, 2001.

J. L. Lumley and G. R. Newman. The return to isotropy of homogeneous turbulence. *J. Fluid Mech.*, 82(1):161–178, 1977.

B. R. Morton, G. I. Taylor, and J. S. Turner. Turbulent gravitational convection from maintained and instantaneous sources. *Proc. R. S. London. Series A.*, 234(1196):1–23, 1956.

J. Penney, Y. Morel, P. H. Haynes, F. Auclair, and C. Nguyen. Diapycnal mixing of passive tracers by Kelvin–Helmholtz instabilities. *J. Fluid Mech.*, 900:A26, 2020.

R. A. Plumb. Tracer interrelationships in the stratosphere. *Rev. Geophys.*, 45(4), 2007.

J. J. Riley and S. M. deBruynKops. Dynamics of turbulence strongly influenced by buoyancy. *Physics of Fluids*, 15(7):2047–2059, 2003.

R. Tailleux and J.-Y. Grandpeix. On the seemingly incompatible parcel and globally integrated views of the energetics of triggered atmospheric deep convection over land. *Q. J. R. Meteorol. Soc.*, 130(604):3223–3243, 2004.

M. van Reeuwijk, P. Salizzoni, G. R. Hunt, and J. Craske. Turbulent transport and entrainment in jets and plumes: A DNS study. *Phys. Rev. Fluids*, 1:074301, 2016.

C. A. Vreugdenhil and J. R. Taylor. Large-eddy simulations of stratified plane couette flow using the anistropic minimum-dissipation model. *Phys. Fluids*, 30(8):085104, 2018.

K. B. Winters and E. A. D'Asaro. Diascalar flux and the rate of fluid mixing. *J. Fluid Mech.*, 317: 179–193, 1996.

K. B. Winters, P. N. Lombard, J. J. Riley, and E. A. D'Asaro. Available potential energy and mixing in density-stratified fluids. *J. Fluid Mech.*, 289: 115–128, 1995.